

A novel multiscale modelling for the hemodynamics in retinal microcirculation with an analytic solution for the capillary-tissue coupled system

Chang Lin^a, Zilong song^b, Bob Eisenburg^c, Shixin Xu^d, Huaxiong Huang^d

^a*School of Mathematical Sciences, Beijing Normal University, Beijing, 100875, China*

^b*Department of Mathematics and Statistics, Utah State University, Logan, 84322, Utah, USA*

^c*Department of Applied Mathematics, Illinois Institute of Technology, Chicago, 60616, Illinois, USA*

^d*Zu Chongzhi Centre, Duke Kunshan University, Kunshan, China*

Abstract

Mathematical modelling of the microcirculatory hemodynamics in the retina is an essential tool for understanding various diseases of the retina, yet remains challenging due to the multiscale nature of the retinal vasculature and its coupling to surrounding tissue. To address this, we develop a multiscale model that couples retinal vasculature across scales with interstitial tissue. Our model combines the one-dimensional (1D) model for arteries and veins with the coupled Darcy equations for capillaries and tissue. The model uses an analytic solution for capillary-tissue coupled system that provides a simple interpretation of the results along with much faster computation. The analytic solution implies a dynamic coupling condition that links the capillary bed with upstream arterial and downstream venous flows. The model is mathematically robust, demonstrated through analysis of the solution's truncation error and convergence. Its predictive accuracy is verified against experimental data and other models, making it useful in interpreting experimental results. Finally, the role of various parameters in controlling retinal hemodynamics is explored.

1. Introduction

The retina is a thin and multilayered neural tissue lining the back of the eye that plays a crucial role in visual function. Its function depends sensitively on adequate blood supply, as retinal hemodynamics helps sustain the metabolism that keeps the retina alive and functional [1]. Disruptions in the hemodynamics can impair oxygen and nutrient delivery, contributing to various retinopathies such as diabetic retinopathy (DR) [1], glaucoma [2, 3, 4] and retinal vascular occlusion [5]. Understanding retinal hemodynamics is thus essential for understanding the life of the retina in health and disease.

Computational modelling serves as a crucial and powerful tool for exploring retinal hemodynamics, integrating physiological processes that are difficult to

measure *in vivo* [6, 7]. Different models have been employed in retinal hemodynamics and oxygenation. Lumped parameter zero-dimensional (0D) models, representing the vasculature as hydraulic resistor circuit [8], have helped to resolve the inconsistencies in clinical data [9]. The 0D accumulated model, in which each segment is modeled as a resistor, is exploited in the simulation of retinal circulation [10, 11]. More complicated models, including the one-dimensional (1D) model, two-dimensional (2D) model and three-dimensional (3D) model, have been used to reveal fundamental properties of oxygen transport in retina [12, 13] as well as deal with properties of disease in specific patients [14, 15, 16, 17]. Existing models provide valuable physiological and pathological insights, however, they focus on specific vascular compartments, including simplifications such as constant capillary pressure or neglecting interactions between capillaries and surrounding tissue. Consequently, very few existing models combine the arteries, veins, capillaries and tissue equally into a comprehensive model. In other tissues, the general rule that all compartments interact with each other has required a systematic structural analysis of flow [18], and the same should hold true for the retina.

A central challenge in modelling the hemodynamics of retinal microcirculation stems from intrinsic multiscale vasculature. Arterial and venous networks display hierarchical tree-like branching [14], while capillaries form an interconnected mesh-like structure [11, 19]. Thus retinal microcirculation inherently constitutes a multiscale system, involving small scale details of flow inside blood vessels and also the large scale layout of the blood vessels. These issues can be addressed using existing methodologies for other organs or tissues [19, 20, 21, 22, 23, 24], where continuum Darcy model for capillary flow is typically coupled to arterial and venous trees via point sources. Even with the point source approximation, the computation is challenging because the Darcy model has to be solved simultaneously with arterial and venous flows [20, 21]. A novel alternative is to use the analytic solution for the capillary flow, which expresses the pressure explicitly so that the Darcy model does not have to be solved in the entire domain. The analytical solution provides significant physical insight as well as much faster computation [19, 22, 23]. However in current analytic methods the fluid exchange between capillaries and tissue is treated approximately. They describe the coupling of capillaries to surrounding tissues using a far-field boundary condition, which serves as a reasonable first step, and a more realistic description of this coupling may be useful.

Our work complements previous studies by developing a novel multiscale model that fully couples retinal vasculature with interstitial tissue. Specifically, the flows in arteries and veins are described by a 1D model [14], while those in capillaries and surrounding tissue are treated as two coupled porous media using Darcy models. The fluid exchange between the capillary and tissue is modelled by source/sink of the two Darcy equations, one for capillary (drainage) and the other for the tissue (feed). Moreover the vasculature is coupled with the capillary in two ways: i) they form the point sources/sinks at artery-capillary and capillary-vein interfaces for the capillary Darcy's equation; and ii) the pressure and flow rate at these point sources/sinks provide the exit conditions for the

arterial vascular tree and the entry conditions for the venous vasculature. What further distinguishes our modelling from others is its analytic solution for the capillary-tissue system, which is derived on a finite domain with a physiological boundary condition. We analyse the convergence and truncation error of the analytical solution extensively to ensure its robustness and accuracy. The analysis of the solution's convergence also reveals some interesting properties of it, which might suggest a new modelling methodology for other tissues. The model is validated against experimental data and other results from existing models. Moreover we demonstrate our model's capability by exploring the effects of parameter variations as well as pulsatile pressure boundary condition.

The rest of the paper is organized as follows. In Section 2 we describe the models and methods, including the 1D model for arteries and veins, synthetic vascular network model, the continuum formulation for the capillary-tissue system, and the derivation of its analytic solution, with discussion on the truncation error. The boundary and multiscale coupling conditions are also specified in this section. In Section 3 the convergence of the solution is analysed extensively, and multiple simulations are performed to assess the model's accuracy and demonstrate its capability. Section 4 consists of the conclusion and discussion.

2. Models and methods

2.1. Network-based simulation for arterial and venous trees

2.1.1. One-dimensional model

The one-dimensional (1D) model is widely adopted to describe the blood flow in the individual vessels of arterial and venous networks. The networks exist in three dimensional space but are often analysed in a two dimensional subset of three dimensional space following the usual conventions of electric circuit theory. For all time $t > 0$ the flow within each vessel is characterized by the flow rate $q(s, t)$ and the cross-sectional area $A(s, t)$ [14, 25], along the axis s of the vessel, and their evolutions are given by

$$\begin{cases} \frac{\partial A}{\partial t} + \frac{\partial q}{\partial s} = 0, \\ \frac{\partial q}{\partial t} + \frac{\partial}{\partial s} \left(\alpha_{cor} \frac{q^2}{A} \right) + \frac{A}{\rho} \frac{\partial p}{\partial s} = f, \end{cases} \quad (1)$$

where α_{cor} is the Coriolis coefficient assumed to describe the velocity profile in each vessel, p is the pressure, ρ is the density of blood and f is the friction term. The coefficient α_{cor} is set as $\alpha_{cor} = 4/3$ which corresponds to the parabolic velocity profile that is consistent with the experimental data in retina [26, 13, 1]. The density is set as $\rho = 1 \text{ g/cm}^3$ from now on in this paper. The explicit form of friction term is given by

$$f = \begin{cases} -8\pi \frac{\eta}{\rho} \frac{q}{A}, & \text{for arteries,} \\ -8\pi \sqrt{\frac{A}{A_0}} \frac{\eta}{\rho} \frac{q}{A}, & \text{for veins,} \end{cases} \quad (2)$$

where $\eta = \eta(r)$ is the dynamical viscosity modelled as a function of the vessel radius r to account for the rheological properties of blood.

The fluid-structure interaction in the problem is captured by following elastic model [27, 28]:

$$p - p_{ext} = K \left[\left(\frac{A}{A_0} \right)^{\beta_1} - \left(\frac{A}{A_0} \right)^{\beta_2} \right], \quad (3)$$

where p_{ext} is the exterior pressure, K is the rigidity being the intrinsic feature of vessel, β_1 and β_2 are parameters depending on the vessel wall behaviour and A_0 is the neutral area of vessel. In the context of retinal vessels, the exterior pressure is identified with the intraocular pressure (IOP), which is the fluid pressure environment surrounding the vessels in the eye. The values of K , β_1 and β_2 varies with the vessel position and its function. The rigidity is

$$K = \begin{cases} \frac{4}{3} \frac{\pi^{1/2} E h}{A_0^{1/2}}, & \text{for arteries,} \\ \frac{1}{9} \frac{\pi^{3/2} E h^3}{A_0^{3/2}}, & \text{for veins.} \end{cases} \quad (4)$$

with E the Young modulus and h the thickness of the vessel wall. The parameters α and β are given by

$$\beta_1 = \begin{cases} 1/2, & \text{for arteries,} \\ 10, & \text{for veins,} \end{cases} \quad (5)$$

and

$$\beta_2 = \begin{cases} 0, & \text{for arteries,} \\ -3/2, & \text{for veins.} \end{cases} \quad (6)$$

The apparent viscosity of blood decreases strongly with the decreasing vessel radius from about 150 μm to about 5 μm , then increases below 5 μm . This unique rheological behaviour is the Fåhræus–Lindqvist effect. To characterize blood's rheological properties, we use an empirical relation developed by Pries *et al.* that expresses viscosity as a function of vessel radius [29, 30, 31]:

$$\eta(r) = \eta_p \left[1 + (\eta_{45} - 1) \left(\frac{r}{r - 0.55} \right)^2 \right] \left(\frac{r}{r - 0.55} \right)^2, \quad (7)$$

where r is the vessel radius, η_p is the viscosity of plasma set as $\eta_p = 0.012$ Poise and η_{45} is the relative apparent blood viscosity for discharge hematocrit of 0.45 given by

$$\eta_{45} = 6 \exp(-0.17r) + 3.2 - 2.44 \exp[-0.06(2r)^{0.645}]. \quad (8)$$

2.1.2. Finite volume method for 1D model

We solve the 1D blood flow model using the finite volume method (FVM) [32, 33]. The governing equations are expressed in conservative form,

$$\frac{\partial \mathbf{U}}{\partial t} + \frac{\partial \mathbf{F}}{\partial s} = \mathbf{S}, \quad (9)$$

where state, flux and source vectors are given by

$$\mathbf{U} = (A, q)^T, \quad (10)$$

$$\mathbf{F} = \left(q, \frac{4}{3} \frac{q^2}{A} + \frac{K}{\rho} \left(\frac{\beta_1}{\beta_1 + 1} \frac{A^{\beta_1 + 1}}{A_0^{\beta_1}} - \frac{\beta_2}{\beta_2 + 1} \frac{A^{\beta_2 + 1}}{A_0^{\beta_2}} \right) \right)^T, \quad (11)$$

$$\mathbf{S} = \left(0, -C_f \frac{q}{A} \right)^T, \quad (12)$$

respectively. The friction coefficient C_f takes different forms for arteries and veins,

$$C_f = \begin{cases} -8\pi \frac{\eta}{\rho}, & \text{for arteries,} \\ -8\pi \sqrt{\frac{A}{A_0}} \frac{\eta}{\rho}, & \text{for veins.} \end{cases}$$

The vessel domain $0 \leq s \leq l_v$ is discretized into $N_s + 1$ spatial points at $s_i = i\Delta s$ with $i = 0, \dots, N_s$ and $\Delta s = l_v/N_s$. The cell centers are located at s_i with $1 \leq i \leq N_s - 1$ where the cells are $C_i = [s_{i-1/2}, s_{i+1/2}] = [(i-1/2)\Delta s, (i+1/2)\Delta s]$, and the boundaries are at $s_0 = 0$ and $s_{N_s} = l_v$, as shown in figure 1. The time is discretized into steps $t_n = n\Delta t$ with $0 \leq n \leq N_t$. The FVM is implemented on C_i over $[t_n, t_{n+1}]$ while boundary conditions are enforced at s_0 and s_{N_s} .

We next describe the FVM for interior points. Integrating equation (9) over the control volume $C_i \times [t_n, t_{n+1}]$ yields to

$$\int_{t_n}^{t_{n+1}} \int_{C_i} \mathbf{S}(s, t) ds dt = \int_{C_i} [\mathbf{U}(s, t_{n+1}) - \mathbf{U}(s, t_n)] ds - \int_{t_n}^{t_{n+1}} [\mathbf{F}(s_{i+1/2}, t) - \mathbf{F}(s_{i-1/2}, t)] dt. \quad (13)$$

The integrals can be approximated as

$$\mathbf{U}_i^{n+1} \approx \frac{1}{\Delta s} \int_{s_{i-1/2}}^{s_{i+1/2}} \mathbf{U}(s, t_{n+1}) ds, \quad (14)$$

$$\mathbf{F}_{i+1/2}^{n+1/2} \approx \frac{1}{\Delta t} \int_{t_n}^{t_{n+1}} \mathbf{F}(s_{i+1/2}, t) dt, \quad (15)$$

$$\frac{1}{2} (\mathbf{S}_{i+1/2}^{n+1/2} + \mathbf{S}_{i-1/2}^{n+1/2}) \approx \int_{t_n}^{t_{n+1}} \int_{s_{i-1/2}}^{s_{i+1/2}} \mathbf{S}(s, t) ds dt, \quad (16)$$

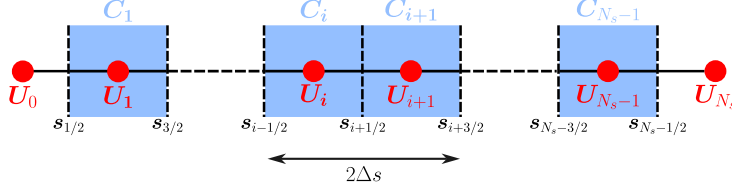


Figure 1: Spatial discretization of vessel.

where $\mathbf{U}_i^{n+1} = \mathbf{U}(s_i, t_{n+1})$, and similar notations are used for flux and source vectors. Thus FVM equation becomes

$$\mathbf{U}_i^{n+1} = \mathbf{U}_i^n - \frac{\Delta t}{\Delta s} \left(\mathbf{F}_{i+1/2}^{n+1/2} - \mathbf{F}_{i-1/2}^{n+1/2} \right) + \frac{\Delta t}{2} \left(\mathbf{S}_{i+1/2}^{n+1/2} + \mathbf{S}_{i-1/2}^{n+1/2} \right). \quad (17)$$

The unknown interface variables $\mathbf{F}_{i+1/2}^{n+1/2}$, $\mathbf{F}_{i-1/2}^{n+1/2}$, $\mathbf{S}_{i+1/2}^{n+1/2}$ and $\mathbf{S}_{i-1/2}^{n+1/2}$ depend on $\mathbf{U}_m^{n+1/2}$ with $m = i \pm 1/2$, which can be determined by the Lax-Wendroff scheme as [32]

$$\mathbf{U}_m^{n+1/2} = \frac{\mathbf{U}_{m+1/2}^n + \mathbf{U}_{m-1/2}^n}{2} + \frac{\Delta t}{2} \left(-\frac{\mathbf{F}_{m+1/2}^n - \mathbf{F}_{m-1/2}^n}{\Delta s} + \frac{\mathbf{S}_{m+1/2}^n + \mathbf{S}_{m-1/2}^n}{2} \right). \quad (18)$$

2.1.3. Synthetic vascular network model

Next we construct a network from the individual vessels. We exploit a Lindenmayer system (L-system) to generate synthetic arterial and venous trees [34]. The model begins with the central retinal artery (CRA) and central retinal vein (CRV), which are positioned at the center of the optic disc. Branches are added iteratively and asymmetrically to create bifurcations up to the fifth order, with lengths given by $l_v = \xi d_v$, where ξ is the length to radius ratio and d_v is the vessel diameter. At each bifurcation boundary one mother vessel is connected to two daughter vessels, and two branching angles θ_1 and θ_2 are determined by [34, 35]

$$\cos \theta_1 = \frac{(1 + v_a^3)^{4/3} + v_a^4 - 1}{2v_a^2(1 + v_a^3)^{2/3}}, \quad (19)$$

$$\cos \theta_2 = \frac{(1 + v_a^3)^{4/3} + 1 - v^4}{2v_a^2(1 + v_a^3)^{2/3}}, \quad (20)$$

where v_a is the asymmetry ratio and normally-distributed noise is added to branching angle values with a standard deviation of $\pi/36$. The vessel radii follow asymmetric branching law

$$r_M^\gamma = r_{d_1}^\gamma + r_{d_2}^\gamma, \quad (21)$$

where r_M , r_{d_1} and r_{d_2} are the radii of mother and two daughter vessels, respectively, and γ is the junction exponent [34, 35]. Generated arterial and venous trees are shown in figure 2(a), where the arterial tree is displayed in red and venous tree is displayed in blue. For comparison, a real retinal vasculature from the DRIVE dataset [36] and its manual segmentation are shown in figure 2(b) and (c), respectively.

Arterioles and venules connecting to arteries and veins are constructed using a structured tree model to set the resistive boundary condition [12, 16, 14]. This boundary condition is defined by the Poiseuille equation for steady, viscous flow, which describes the relation between flow and pressure, given by

$$p_{up} - p_{down} = Rq, \quad (22)$$

where p_{up} and p_{down} are the upstream and downstream pressures, R is the resistance and q is flow rate.

In the structured tree model arterioles and venules would grow from terminal vessels until their radii are decreased to $r = 6 \mu\text{m}$, which is the characteristic radius of capillary [37, 21], and the branching is performed similarly as that in L-system [14]. Then the equivalent resistance of root vessels are calculated recursively for resistive boundary condition. For a vessel M with its own resistance R_M and its daughter vessels with resistances $R_{d_1,eq}$ and $R_{d_2,eq}$, the total equivalent resistance is

$$R_{M,eq} = R_M + R_{d,eq}, \quad (23)$$

where

$$\frac{1}{R_{d,eq}} = \frac{1}{R_{d_1,eq}} + \frac{1}{R_{d_2,eq}}. \quad (24)$$

The resistance of a vessel is given by

$$R_k = \frac{8\eta_k l_k}{\pi r_k^4}, \quad (25)$$

where the viscosity η_k is computed by the Pries *et al.*'s model and the length is $l_k = \xi r_k$.

2.2. Continuum formulation for the capillary network and surrounding tissue

2.2.1. Capillary-tissue coupled system

The retina can be modelled as a porous medium since it is composed of cells, fibres and interstitial space filled with a fluid. The capillary bed is distributed in this environment, and it forms a dense plexus through which the blood can flow, rather than being a collection of a few discrete, isolated branches. The composite structure of capillary bed and surrounding tissue is topologically analogous to a porous material, where the solid matrix comprises tissue's extracellular matrix fused with capillary walls and the intravascular space of capillaries forms

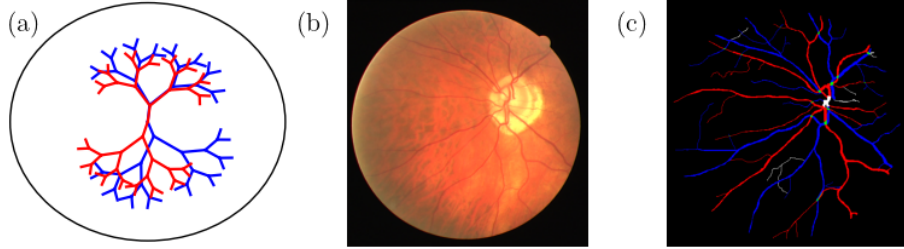


Figure 2: Synthetic and real retinal vasculature. (a) The arterial (red) and venous (blue) trees in retinal tissue (black circle) generated using an L-system. (b) Fundus image from DRIVE dataset [36]. (c) The manually segmented retinal vasculature for (b). Arteries and veins are displayed in red and blue, respectively. The green denotes pixels classified as both artery and vein and the white denotes the uncertain segment.

a continuous, interconnected pore space. Given bidirectional hemodynamic exchange between capillaries and surrounding tissue, the two systems should be combined in the same way that electrical systems are combined in electrical models of syncytial tissue [18]. We thus model the capillary bed and surrounding tissue as interacting porous media. The flow in both the capillary bed and surrounding tissue is modelled as a Darcy flow [22, 19, 20, 21]. The Darcy flux of capillaries \mathbf{u}_{cap} , i.e., volumetric flow rate per unit area (in unit cm/s), is given by

$$\mathbf{u}_{cap} = -\frac{1}{\mu_{cap}} \mathbf{k}_{cap} \cdot \nabla p_{cap} \quad \text{in } \Omega_t, \quad (26)$$

where \mathbf{k}_{cap} is the permeability tensor (in unit cm²), μ_{cap} is the viscosity of blood and p_{cap} is the pressure of capillary network. The equation (26) states that the flow in capillaries is mainly driven by the pressure gradient, which is consistent with flow characteristics in retinal vasculature physiologically. The capillary network is assumed isotropic and homogeneous [20, 38] such that the permeability tensor is $\mathbf{k}_{cap} = k_{cap} \mathbf{I}$, where \mathbf{I} is the identity matrix. Since the blood is incompressible conservation of mass yields to

$$\nabla \cdot \mathbf{u}_{cap} = \psi_{cap} \quad \text{in } \Omega_t, \quad (27)$$

where ψ_{cap} is the source term (in unit s⁻¹). Combining equations (26) and (27) the flow in capillaries is characterized by following equation

$$-\frac{k_{cap}}{\mu_{cap}} \nabla^2 p_{cap} = \psi_{cap}(\mathbf{x}) \quad \text{in } \Omega_t. \quad (28)$$

The source term should combine three key components: arterial inflow, venous drainage and the fluid exchange between capillaries and surrounding tissue, which is expressed as

$$\psi_{cap}(\mathbf{x}) = \psi_{ac} + \psi_{cv} - \psi_{ct}, \quad (29)$$

where ψ_{ac} , ψ_{cv} and ψ_{ct} denote arterial inflow, venous drainage and fluid exchange between capillaries and the tissue, respectively. The contributions of arterial and venous trees are modeled as the summation of discrete point sources:

$$\psi_{ac}(\mathbf{x}) + \psi_{cv}(\mathbf{x}) = \sum_{n=1}^{N_{cap}} q_n \delta(\mathbf{x} - \mathbf{x}_n), \quad (30)$$

where N_{cap} is the total number of point sources, q_n represents the flow rate of source/sink at location \mathbf{x}_n and $\delta(\cdot)$ is the Dirac delta function. The fluid exchange between capillaries and tissue is mainly determined by their hydrostatic and osmotic pressures. Using the Starling's filtration principle the fluid filtration rate is given by [39, 21]

$$\psi_{ct}(\mathbf{x}) = L_h \times S \times [(p_{cap}(\mathbf{x}) - p_t(\mathbf{x})) - \alpha_r(\pi_{cap}(\mathbf{x}) - \pi_t(\mathbf{x}))], \quad (31)$$

where L_h is the hydraulic conductivity of capillary wall, S is the surface area, p_t is the tissue pressure in retinal layers, π_{cap} is capillary plasma osmotic pressure, π_t is interstitial fluid osmotic pressure and α_r is the permeability of capillary wall to proteins. Due to the tight junctions of the blood-retina barrier (BRB), which make capillary wall largely impermeable to plasma proteins, the osmotic term could be neglected and the term ψ_{ct} can be modelled as a drainage system [40]:

$$\psi_{ct}(\mathbf{x}) = \alpha \times (p_{cap}(\mathbf{x}) - p_t(\mathbf{x})), \quad (32)$$

where $\alpha = L_h \times S$ is the drainage rate (in unit $\text{cm} \cdot \text{s/g}$). This simplification is also used by the models for other tissues that are more permeable to proteins [21], and has been shown to produce physiologically consistent results. Similarly the tissue pressure satisfies

$$-\frac{k_t}{\mu_t} \nabla^2 p_t = \psi_{ct}, \quad \text{in } \Omega_t, \quad (33)$$

where k_t is the tissue permeability and μ_t is the viscosity of interstitial fluid in tissue. Thus the capillary-tissue coupled system is given by [38]

$$\begin{cases} -\frac{k_{cap}}{\mu_{cap}} \nabla^2 p_{cap} = \sum_{n=1}^{N_{cap}} q_n \delta(\mathbf{x} - \mathbf{x}_n) - \alpha(p_{cap} - p_t) & \text{in } \Omega_t, \\ -\frac{k_t}{\mu_t} \nabla^2 p_t = \alpha(p_{cap} - p_t) & \text{in } \Omega_t, \end{cases} \quad (34)$$

which is subject to following boundary conditions

$$\begin{cases} -\frac{k_{cap}}{\mu_{cap}} \nabla p_{cap} \cdot \mathbf{n} = 0 & \text{on } \partial \Omega_t, \\ -\frac{k_t}{\mu_t} \nabla p_t \cdot \mathbf{n} = 0 & \text{on } \partial \Omega_t. \end{cases} \quad (35)$$

Previous studies usually assume an idealized geometry of the tissue domain Ω_t , such as a sphere [7, 15, 17], a circular domain with radial cuts [11, 10], or a circular disk [13], which is motivated by the spherical anatomy of the retina. Following this precedent, we assume a circular domain of radius R_t for the tissue, and it approximates the region of the tissue with small curvature where retinal vasculature is distributed. The boundary conditions (35) are crucial. Physiologically, neither blood nor interstitial fluid flows across the boundary $\partial\Omega_t$. For capillaries, the flux of blood across the boundary is described by $-(k_{cap}/\mu_{cap})\nabla p_{cap} \cdot \mathbf{n}$, and enforcing this flux to be zero implies the physiological no-flow condition, i.e., the first boundary condition. Implementing the same requirement to the interstitial fluid in tissue yields the boundary condition for p_t . Moreover these two boundary conditions correspond to two fundamental conservation laws. First, integrating the boundary condition for p_t over $\partial\Omega_t$ yields to

$$\int_{\partial\Omega_t} -\frac{k_t}{\mu_t} \nabla p_t \cdot \mathbf{n} ds = \int_{\Omega_t} -\frac{k_t}{\mu_t} \nabla^2 p_t d\mathbf{x} = \int_{\Omega_t} \alpha(p_{cap} - p_t) d\mathbf{x} = 0, \quad (36)$$

which implies that

$$\int_{\Omega_t} p_{cap} d\mathbf{x} = \int_{\Omega_t} p_t d\mathbf{x}. \quad (37)$$

This equality states the tissue fluid homeostasis, where net filtration is balanced by net reabsorption such that there is no pathological fluid accumulation in interstitium. In other words, the areas where $p_{cap} > p_t$ are balanced by the areas where $p_{cap} < p_t$, which implies the conservation of fluid volume for the tissue. Second, integrating the boundary condition for p_{cap} implies

$$\int_{\partial\Omega_t} -\frac{k_{cap}}{\mu_{cap}} \nabla p_{cap} \cdot \mathbf{n} ds = \int_{\Omega_t} \psi_{cap} d\mathbf{x} = \sum_{n=1}^{N_{cap}} q_n - \alpha \int_{\Omega_t} (p_{cap} - p_t) d\mathbf{x}, \quad (38)$$

thus the boundary condition that $-(k_{cap}/\mu_{cap})\nabla p_{cap} \cdot \mathbf{n} = 0$ is satisfied only if $\sum_n q_n = 0$, which states the conservation of mass.

2.2.2. Solutions to capillary-tissue coupled system

To solve the capillary-tissue coupled system we begin with writing the equations in matrix form

$$-\nabla^2 \begin{bmatrix} p_{cap} \\ p_t \end{bmatrix} = \mathbf{C} \begin{bmatrix} p_{cap} \\ p_t \end{bmatrix} + \begin{bmatrix} \frac{1}{a} \sum_n q_n \delta(\mathbf{x} - \mathbf{x}_n) \\ 0 \end{bmatrix}, \quad (39)$$

where the matrix \mathbf{C} is given by

$$\mathbf{C} = \alpha \begin{bmatrix} -1/a & 1/a \\ 1/b & -1/b \end{bmatrix}, \quad (40)$$

and $a = k_{cap}/\mu_{cap}$ and $b = k_t/\mu_t$ are the hydraulic conductivities for capillaries and tissue (in unit $\text{cm} \cdot \text{s/g}$), respectively. The system is decoupled via the following transformation to new variables:

$$\begin{bmatrix} p_{mean} \\ p_{exch} \end{bmatrix} = \mathbf{T} \begin{bmatrix} p_{cap} \\ p_t \end{bmatrix}, \quad (41)$$

where p_{mean} is the conductivity weighted average pressure, p_{exch} is the exchange pressure proportional to their difference, and \mathbf{T} is the transformation matrix given by

$$\mathbf{T} = \frac{a}{a+b} \begin{bmatrix} 1 & b/a \\ -1 & 1 \end{bmatrix}. \quad (42)$$

The resulting decoupled system is then given by

$$\begin{cases} -\nabla^2 p_{mean} = \frac{1}{a+b} \sum_{n=1}^{N_{cap}} q_n \delta(\mathbf{x} - \mathbf{x}_n) & \text{on } \partial\Omega_t, \\ -\nabla^2 p_{exch} + \lambda^2 p_{exch} = -\frac{1}{a+b} \sum_{n=1}^{N_{cap}} q_n \delta(\mathbf{x} - \mathbf{x}_n) & \text{on } \partial\Omega_t, \end{cases} \quad (43)$$

where $\lambda = \sqrt{\alpha(1/a + 1/b)}$ and the system is subject to the boundary conditions

$$\begin{cases} \nabla p_{mean} \cdot \mathbf{n} = 0 & \text{on } \partial\Omega_t, \\ \nabla p_{exch} \cdot \mathbf{n} = 0 & \text{on } \partial\Omega_t. \end{cases} \quad (44)$$

Once the decoupled system are solved the capillary and tissue pressures can be obtained through the inverse transformation that

$$\begin{bmatrix} p_{cap} \\ p_t \end{bmatrix} = \mathbf{T}^{-1} \begin{bmatrix} p_{mean} \\ p_{exch} \end{bmatrix} = \begin{bmatrix} p_{mean} - \frac{b}{a} p_{exch} \\ p_{mean} + p_{exch} \end{bmatrix}, \quad (45)$$

where \mathbf{T}^{-1} is the inverse transformation matrix given by

$$\mathbf{T}^{-1} = \begin{bmatrix} 1 & -b/a \\ 1 & 1 \end{bmatrix}. \quad (46)$$

To solve the decoupled system, we solve its adjoint problems. The adjoint problem for p_{mean} is given by [41, 42]

$$\begin{cases} \nabla'^2 f_{mean}(\mathbf{x}, \mathbf{x}') = \delta(\mathbf{x} - \mathbf{x}') & \text{in } \Omega_t, \\ \nabla' f_{mean}(\mathbf{x}, \mathbf{x}') \cdot \mathbf{n}' = 1/S & \text{on } \partial\Omega_t, \end{cases} \quad (47)$$

where $S = 2\pi R_t$ is the length of the boundary $\partial\Omega_t$. To construct the solution, a image point source is added at $\mathbf{x}'' \in \mathbb{R}^2 \setminus \Omega_t$, where $\mathbf{x}'' = (R_t^2/|\mathbf{x}|^2)\mathbf{x}$. The general solution to the adjoint problem is then given by

$$f_{mean}(\mathbf{x}, \mathbf{x}') = \frac{1}{2\pi} (\log |\mathbf{x}' - \mathbf{x}| + k \log |\mathbf{x}' - \mathbf{x}''| + c), \quad (48)$$

where k and c are the constants left to be determined. The normal derivative is computed as

$$\begin{aligned}\nabla' f_{mean}(\mathbf{x}, \mathbf{x}') \cdot \mathbf{n}' &= \frac{1}{2\pi} \left[\frac{\mathbf{x}' - \mathbf{x}}{|\mathbf{x}' - \mathbf{x}|^2} + \frac{k(\mathbf{x}' - \mathbf{x}'')}{|\mathbf{x}' - \mathbf{x}''|^2} \right] \cdot \frac{\mathbf{x}'}{|\mathbf{x}'|} \\ &= \frac{1}{2\pi|\mathbf{x}'|} \left[\frac{|\mathbf{x}'|^2 - \mathbf{x} \cdot \mathbf{x}'}{|\mathbf{x}' - \mathbf{x}|^2} + \frac{k|\mathbf{x}'|^2 - k\mathbf{x}' \cdot \mathbf{x}''}{|\mathbf{x}' - \mathbf{x}''|^2} \right],\end{aligned}\quad (49)$$

and on the boundary $\partial\Omega_t$, where $|\mathbf{x}'| = R_t$. The expression simplifies to

$$\nabla' f_{mean}(\mathbf{x}, \mathbf{x}') \cdot \mathbf{n}' = \frac{1}{2\pi R_t} \frac{1}{|\mathbf{x}' - \mathbf{x}|^2} [|\mathbf{x}'|^2 + k|\mathbf{x}|^2 - (k+1)\mathbf{x}' \cdot \mathbf{x}].\quad (50)$$

We can obtain the mean pressure by enforcing the boundary condition in problem (47) to solve for k . The derivation is provided in appendix Appendix A.

The mean pressure p_{mean} is given by

$$p_{mean}(\mathbf{x}) = -\frac{1}{a+b} \sum_{n=1}^{N_{cap}} q_n f_{mean}(\mathbf{x}, \mathbf{x}_n) + \overline{p_{mean}},\quad (51)$$

where the boundary average $\overline{p_{mean}}$ is given by

$$\overline{p_{mean}} = \frac{1}{S} \int_{\partial\Omega_{cap}} p_{mean}(\mathbf{x}') ds'.\quad (52)$$

We write the variable p_{mean} in polar coordinates as

$$p_{mean}(r, \theta) = -\frac{1}{a+b} \sum_{n=1}^{N_{cap}} q_n f_{mean}(r, \theta; r_n, \theta_n) + \overline{p_{mean}},\quad (53)$$

where the function $f_{mean}(r, \theta; r_n, \theta_n)$ is given by

$$\begin{aligned}f_{mean}(r, \theta; r_n, \theta_n) &= \frac{1}{4\pi} \log(r_n^2 + r^2 - 2r_n r \cos(\theta_n - \theta)) \\ &+ \frac{1}{4\pi} \log\left(r_n^2 + \frac{R_t^4}{r^2} - 2r_n \frac{R_t^2}{r} \cos(\theta_n - \theta)\right).\end{aligned}\quad (54)$$

When implementing the solution for p_{mean} , the conservation of mass should be enforced explicitly, which is given by

$$0 = \sum_{n=1}^{N_{cap}} q_n.\quad (55)$$

That is, the total flow entering capillary bed from arterial tree equals to the total flow drained into veins. To derive equation (55) we integrate p_{mean} over the boundary and obtain

$$\overline{p_{mean}} = -\frac{1}{S} \frac{1}{a+b} \sum_{n=1}^{N_{cap}} q_n \int_{\partial\Omega_t} f_{mean}(r, \theta; r_n, \theta_n) ds + \overline{p_{mean}},\quad (56)$$

which implies the consistent condition for p_{mean} that

$$0 = -\frac{1}{S} \frac{1}{a+b} \sum_{n=1}^{N_{cap}} q_n \int_{\partial\Omega_t} f_{mean}(r, \theta; r_n, \theta_n) ds. \quad (57)$$

This demonstrates that the total flow is balanced, with each q_n weighted by its respective boundary integral. In other words the boundary integral quantifies how any local flow source disturbs the averaged pressure. Interestingly, evaluation of the boundary integral shows it is independent of the source location:

$$\int_{\partial\Omega_t} f_{mean}(r, \theta; r_n, \theta_n) ds = 2R_t \log R_t, \quad (58)$$

and a detailed computation for the boundary integral is provided in appendix Appendix B. Thus the equation (57) can be simplified to equation (55). The identical value of boundary integral for each source demonstrates that each connection to the larger vasculature, whether an feeding arteriole or a draining venule, contributes equally to the balance, which is consistent to the physiological situation that capillary plexus is highly interconnected.

The adjoint problem for variable p_{exch} is given by

$$\begin{cases} \nabla^2 f_{exch}(\mathbf{x}, \mathbf{x}_n) - \lambda^2 f_{exch}(\mathbf{x}, \mathbf{x}_n) = \delta(\mathbf{x} - \mathbf{x}_n) & \text{in } \Omega_t, \\ \nabla f_{exch}(\mathbf{x}, \mathbf{x}_n) \cdot \mathbf{n} = 0 & \text{on } \partial\Omega_t, \end{cases} \quad (59)$$

whose solution enables to express p_{exch} as

$$p_{exch}(\mathbf{x}) = \frac{1}{a+b} \sum_{n=1}^{N_{cap}} q_n f_{exch}(\mathbf{x}, \mathbf{x}_n). \quad (60)$$

The equation of adjoint problem in polar coordinates is given by

$$\frac{1}{r} \frac{\partial}{\partial r} \left(r \frac{\partial f_{exch}}{\partial r} \right) + \frac{1}{r^2} \frac{\partial^2 f_{exch}}{\partial \theta^2} - \lambda^2 f_{exch} = \frac{\delta(r - r_n) \delta(\theta - \theta_n)}{r}, \quad (61)$$

and substituting the trail solution $f_{exch}(r, \theta; r_n, \theta_n) = R(r)\Theta(\theta)$ leads to

$$\frac{r}{R(r)} \frac{\partial}{\partial r} \left(r \frac{\partial R(r)}{\partial r} \right) + \frac{1}{\Theta(\theta)} \frac{\partial^2 \Theta(\theta)}{\partial \theta^2} - \lambda^2 r^2 = 0 \quad (62)$$

as $(r, \theta) \neq (r_n, \theta_n)$, which yields to

$$\frac{d^2 \Theta}{d\theta^2} + m^2 \Theta = 0, \quad (63)$$

whose solution is composed of $\exp(im\theta)$ and $\exp(-im\theta)$. Together with the Fourier expansion of $\delta(\theta - \theta_n)$ that

$$\delta(\theta - \theta_n) = \frac{1}{2\pi} \sum_{m=-\infty}^{\infty} \exp[im(\theta - \theta_n)], \quad (64)$$

we thus assume the solution is

$$f_{exch}(r, \theta; r_n, \theta_n) = \frac{1}{2\pi} \sum_{m=-\infty}^{\infty} R_m(r) \exp[im(\theta - \theta_n)], \quad (65)$$

which yields to following eigenvalue problem

$$\frac{1}{r} \frac{d}{dr} \left(r \frac{dR_m}{dr} \right) - \left(\frac{m^2}{r^2} + \lambda^2 \right) R_m = \frac{\delta(r - r_n)}{r}. \quad (66)$$

The equation (66) is a modified Bessel equation and its general solution, which must remain finite at $r = 0$, is given by

$$R_m(r) = \begin{cases} A_m I_m(\lambda r), & r \leq r_n, \\ B_m I_m(\lambda r) + C_m K_m(\lambda r), & r > r_n, \end{cases} \quad (67)$$

where $I_m(\lambda r)$ and $K_m(\lambda r)$ are the modified Bessel functions of order m and A_m , B_m as well as C_m are the coefficients left to determine, and a detailed computation for them is provided in appendix Appendix C. The radial component in equation (65) is given by

$$R_{m,n}(r) = I_m(\lambda r_{<}) \left[\frac{K'_m(\lambda R_t)}{I'_m(\lambda R_t)} I_m(\lambda r_{>}^n) - K_m(\lambda r_{>}^n) \right], \quad (68)$$

with $r_{<}^n = \min(r, r_n)$ and $r_{>}^n = \max(r, r_n)$. We assume the convergence of this series solution, which will be addressed in following section. Plugging the expression of f_{exch} with equation (68) into equation (60) yields to

$$p_{exch}(r, \theta) = \frac{1}{2\pi(a+b)} \sum_{n=1}^{N_{cap}} \sum_{m=-\infty}^{\infty} q_n R_{m,n}(r) \exp[im(\theta - \theta_n)]. \quad (69)$$

With solutions to mean and exchange pressures capillary pressure is given by

$$p_{cap}(r, \theta) = p_{mean} - \frac{b}{a} p_{exch} = -\frac{1}{a+b} \sum_{n=1}^{N_{cap}} q_n (f_{mean} + \frac{b}{a} f_{exch}). \quad (70)$$

We denote the modified Green's function for capillary pressure as

$$G(r, \theta; r_n, \theta_n) = f_{mean}(r, \theta; r_n, \theta_n) + \frac{b}{a} f_{exch}(r, \theta; r_n, \theta_n), \quad (71)$$

and express the capillary pressure as

$$p_{cap}(r, \theta) = -\frac{1}{a+b} \sum_{n=1}^{N_{cap}} q_n G(r, \theta; r_n, \theta_n). \quad (72)$$

Tissue pressure is given by

$$p_t(r, \theta) = p_{mean} + p_{exch} = -\frac{1}{a+b} \sum_{n=1}^{N_{cap}} q_n (f_{mean} - f_{exch}). \quad (73)$$

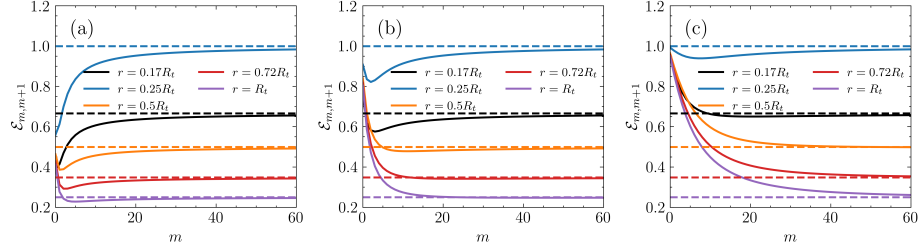


Figure 3: The dependence of relative ratio $\mathcal{E}_{m,m+1}$ on the order m for $r_n = 0.25R_t$. Solid lines denote the values of relative ratio while dashed lines are the upper bound. Different colours correspond to various values of radial coordinate. (a) Value of drainage rate is of $\alpha = 2 \times 10^{-9}$ cm · s/g. (b) Value of drainage rate is of $\alpha = 2 \times 10^{-8}$ cm · s/g. (c) Value of drainage rate is of $\alpha = 2 \times 10^{-7}$ cm · s/g. Other parameter values are $k_{cap} = 2 \times 10^{-9}$ cm² and $k_t = 2 \times 10^{-12}$ cm².

2.2.3. Numerical treatments of logarithmic singularity and infinite summation

Both of the logarithmic singularity and the infinite summation could lead to numerical issues, and in what follows we show how to address the problems.

The singular behaviour of the logarithmic solution is resolved via local domain averaging. The average of the logarithmic function can be written as

$$\langle \log |\mathbf{x} - \mathbf{x}_n| \rangle = \frac{1}{A_n} \int_{\Omega_n} f(\mathbf{x}) \log |\mathbf{x} - \mathbf{x}_n| d\mathbf{x}, \quad (74)$$

where $f(\mathbf{x})$ is the weight function, Ω_n is the averaged domain and A_n is its area. The simplest average could be the one with the circular domain and weight function $f(\mathbf{x}) = 1$, and the circular domain is centered at the position of point source $\mathbf{x} = \mathbf{x}_n$ with vessel radius $r_{v,n}$. The integral for this average could be computed as follows:

$$\int_{\Omega_n} \log |\mathbf{x} - \mathbf{x}_n| d\mathbf{x} = 2\pi \int_0^{r_{v,n}} r \log r dr = \pi \left[r_{v,n}^2 \log r_{v,n} - \frac{1}{2} r_{v,n}^2 \right], \quad (75)$$

where Ω_n is a circular domain, thus the resulting averaged value is given by

$$\langle \log |\mathbf{x} - \mathbf{x}_n| \rangle = \log r_{v,n} - \frac{1}{2}. \quad (76)$$

The finite order truncation of f_{exch} is utilized in computations. The truncation with order M is given by

$$f_{exch}(r, \theta; r_n, \theta_n) = \frac{1}{2\pi} \sum_{m=-M}^M R_m(r) \exp[im(\theta - \theta_n)], \quad (77)$$

since the radial component is symmetric in m the truncation can be written as

$$f_{exch}(r, \theta; r_n, \theta_n) = \frac{1}{2\pi} R_{0,n}(r) + \frac{1}{\pi} \sum_{m=1}^M R_{m,n}(r) \cos[m(\theta - \theta_n)], \quad (78)$$

and the truncation error is given by

$$\mathcal{E}_M = \frac{1}{\pi} \sum_{m=M+1}^{\infty} R_{m,n}(r) \cos[m(\theta - \theta_n)]. \quad (79)$$

We next explore the accuracy of this truncation by analysing the decay of higher-order terms. To characterize it we analyse the relative ratio between radial components $R_{m,n}$ and $R_{m+1,n}$, defined as

$$\mathcal{E}_{m,m+1} = \frac{|R_{m+1,n}(r)|}{|R_{m,n}(r)|}, \quad (80)$$

and for $0 \leq r < R_t$ the term $K'_m(\lambda R_t) I_m(\lambda r^n) / I'_m(\lambda R_t)$ can be neglected compared to the term $K_m(\lambda r^n)$ as $m \rightarrow \infty$, as discussed in appendix Appendix D, thus the relative ratio asymptotically can be approximated as

$$\mathcal{E}_{m,m+1} \simeq \frac{K_{m+1}(\lambda r^n)}{K_m(\lambda r^n)} \frac{I_{m+1}(\lambda r^n)}{I_m(\lambda r^n)}. \quad (81)$$

Then using the inequalities that [43, Theorems 2 and 7]

$$\frac{K_{m+1}(\lambda r)}{K_m(\lambda r)} < \frac{m + \frac{1}{2} + \sqrt{(m + \frac{1}{2})^2 + (\lambda r)^2}}{\lambda r}, \quad m \geq -1/2 \quad (82)$$

$$\frac{I_{m+1}(\lambda r)}{I_m(\lambda r)} < \frac{\lambda r}{m + \frac{1}{2} + \sqrt{(m + \frac{1}{2})^2 + (\lambda r)^2}}, \quad m \geq -1/2, \quad (83)$$

we obtain that

$$\mathcal{E}_{m,m+1} < \frac{m + \frac{1}{2} + \sqrt{(m + \frac{1}{2})^2 + (\lambda r^n)^2}}{m + \frac{1}{2} + \sqrt{(m + \frac{1}{2})^2 + (\lambda r^n)^2}} \frac{r^n}{r^n}, \quad (84)$$

thus for all r and significantly large m the ratio satisfies

$$\mathcal{E}_{m,m+1} < \frac{\min\{r, r_n\}}{\max\{r, r_n\}} \leq 1. \quad (85)$$

Figure 3 illustrates the dependence of relative ratio on the order m , where solid lines represent the values of relative ratio and dashed lines are the upper bound $\min\{r, r_n\} / \max\{r, r_n\}$, and different colours correspond to various values of radial coordinate. Results are shown for drainage rates of $\alpha = 2 \times 10^{-9} \text{ cm} \cdot \text{s/g}$, $\alpha = 2 \times 10^{-8} \text{ cm} \cdot \text{s/g}$ and $\alpha = 2 \times 10^{-7} \text{ cm} \cdot \text{s/g}$. When m increases, the relative ratio approaches to the upper bound but remains strictly below it. As drainage rate becomes larger, as shown in figure 4, the convergence of relative ratio toward the bound is slower, but the ratio is still less than 1, which demonstrates that the series term still decay exponentially. Thus we

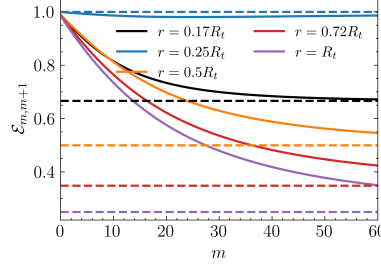


Figure 4: The dependence of relative ratio $\mathcal{E}_{m,m+1}$ on the order m for $r_n = 0.25R_t$. Solid lines denote the values of relative ratio while dashed lines are the upper bound. Different colours correspond to various values of radial coordinate. The drainage rate is $\alpha = 2 \times 10^{-6} \text{ cm} \cdot \text{s/g}$.



Figure 5: Two different bifurcation boundaries.

obtain $R_{m,n}(r) \leq R_{0,n}(r)(\min\{r, r_n\} / \max\{r, r_n\})^m$ and following estimate for the truncation error:

$$\mathcal{E}_M \leq \frac{1}{\pi} \sum_{m=M+1}^{\infty} |R_{m,n}(r)| \leq \frac{1}{\pi} |R_{0,n}(r)| \sum_{m=M+1}^{\infty} \left(\frac{\min\{r, r_n\}}{\max\{r, r_n\}} \right)^m. \quad (86)$$

For any $r \neq r_n$ the series $\sum_{m=M+1}^{\infty} (\min\{r, r_n\} / \max\{r, r_n\})^m$ converges, then the truncation error satisfies

$$\mathcal{E}_M \leq \frac{1}{\pi} |R_{0,n}(r)| \frac{(\min\{r, r_n\} / \max\{r, r_n\})^M}{1 - (\min\{r, r_n\} / \max\{r, r_n\})}. \quad (87)$$

Thus the exponential decay of relative ratio ensures high accuracy even with only a few terms. Although a larger drainage rate slows the convergence of relative ratio to the upper bound, the ratio remains strictly below 1 as well, and $|R_{0,n}(r)|$ is relatively small, as a result, the truncation for large drainage rate with only a few terms could also have high accuracy.

2.3. Boundary and multiscale coupling conditions

It remains to specify the boundary conditions for the 1D model, as well as the coupling conditions at the interfaces where arterioles and venules are connected to the capillaries. The following sections describe these conditions and their numerical implementations.

2.3.1. Boundary conditions for vascular trees

The pressure boundary conditions are imposed at the CRA inlet and CRV outlet. While the pressure at CRA could be constant or time-dependent, that at CRV outlet is set constant. At the CRA inlet, the area $A_{CRA,0}^{n+1}$ is determined by solving the equation

$$p_{in,CRA}(t_{n+1}) - p_{ext} = K \left[\left(\frac{A_{CRA,0}^{n+1}}{A_0} \right)^{\beta_1} - \left(\frac{A_{CRA,0}^n}{A_0} \right)^{\beta_2} \right], \quad (88)$$

where $p_{in,CRA}(t_{n+1})$ is the prescribed inlet pressure at CRA. The corresponding flow rate is computed by discretizing the mass-conservation equation [44]

$$\frac{(A_{CRA,0}^{n+1} + A_{CRA,1}^{n+1}) - (A_{CRA,0}^n + A_{CRA,1}^n)}{2\Delta t} + \frac{q_{CRA,1}^{n+1} - q_{CRA,0}^{n+1}}{\Delta s_{CRA}} = 0, \quad (89)$$

which yields the following

$$q_{CRA,0}^{n+1} = q_{CRA,1}^{n+1} + \frac{\Delta s_{CRA}}{2\Delta t} \left[(A_{CRA,0}^{n+1} + A_{CRA,1}^{n+1}) - (A_{CRA,0}^n + A_{CRA,1}^n) \right]. \quad (90)$$

Similarly, at the CRV outlet, the area $A_{CRV,0}^{n+1}$ is computed from

$$p_{out,CRV} - p_{ext} = K \left[\left(\frac{A_{CRV,0}^{n+1}}{A_0} \right)^{\beta_1} - \left(\frac{A_{CRV,0}^n}{A_0} \right)^{\beta_2} \right], \quad (91)$$

where $p_{out,CRV}$ is the CRV outlet pressure. The mass-conservation equation combined with the constant CRV outlet pressure implies that $\partial q/\partial s = 0$, and the flow rate at CRV outlet is thus determined by

$$q_{CRV,0}^{n+1} = q_{CRV,1}^{n+1}. \quad (92)$$

The bifurcation boundary conditions are governed by following equations [45]:

$$\begin{cases} q_M - q_{d_1} - q_{d_2} = 0, \\ p_M - p_{d_1} = 0, \\ p_M - p_{d_2} = 0, \\ \frac{\partial A_M}{\partial t} + \frac{\partial q_M}{\partial s_M} = 0, \\ \frac{\partial A_{d_1}}{\partial t} + \frac{\partial q_{d_1}}{\partial s_{d_1}} = 0, \\ \frac{\partial A_{d_2}}{\partial t} + \frac{\partial q_{d_2}}{\partial s_{d_2}} = 0, \end{cases} \quad (93)$$

where the subscripts M , d_1 and d_2 denote the mother and two daughter vessels, respectively. These conditions are identical for different shapes of bifurcation

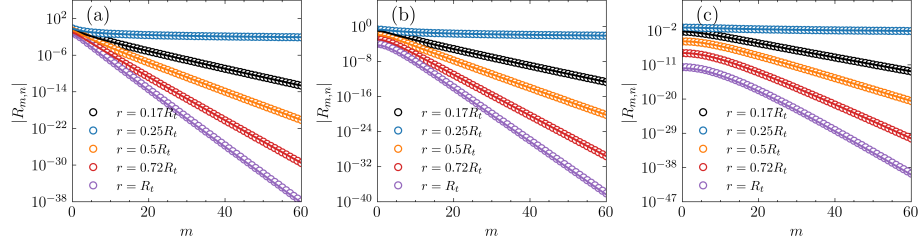


Figure 6: The dependence of radial component $R_{m,n}$ on the order m for $r_n = 0.25R_t$. Circles are the exact values of radial component computed by equation (68) while lines denote the approximation (126). Different colours correspond to various values of radial coordinate. (a) Value of drainage rate is of $\alpha = 2 \times 10^{-9}$ cm · s/g. (b) Value of drainage rate is of $\alpha = 2 \times 10^{-8}$ cm · s/g. (c) Value of drainage rate is of $\alpha = 2 \times 10^{-7}$ cm · s/g. Other parameter values are $k_{cap} = 2 \times 10^{-9}$ cm² and $k_t = 2 \times 10^{-12}$ cm².

boundary, as shown in figure 5. The mass-conservation equations are discretized, which yields to following system at $t = t_{n+1}$, and the boundary condition at $t = t_{n+1}$ is [44, 45]

$$\mathbf{Y}(\mathbf{x}_b) = [Y_1(\mathbf{x}_b), Y_2(\mathbf{x}_b), \dots, Y_6(\mathbf{x}_b)] = \mathbf{0}, \quad (94)$$

where

$$Y_1 = q_{M,N_s}^{n+1} - q_{d_1,0}^{n+1} - q_{d_2,0}^{n+1}, \quad (95)$$

$$Y_2 = p_{M,N_s}^{n+1}(A_{M,N_s}^{n+1}) - p_{d_1,0}^{n+1}(A_{d_1,0}^{n+1}), \quad (96)$$

$$Y_3 = p_{M,N_s}^{n+1}(A_{M,N_s}^{n+1}) - p_{d_2,0}^{n+1}(A_{d_2,0}^{n+1}), \quad (97)$$

$$Y_4 = \frac{(A_{M,N_s}^{n+1} + A_{M,N_s-1}^{n+1}) - (A_{M,N_s}^n + A_{M,N_s-1}^n)}{2\Delta t} + \frac{q_{M,N_s}^{n+1} - q_{M,N_s-1}^{n+1}}{\Delta s_M}, \quad (98)$$

$$Y_5 = \frac{(A_{d_1,0}^{n+1} + A_{d_1,1}^{n+1}) - (A_{d_1,0}^n + A_{d_1,1}^n)}{2\Delta t} + \frac{q_{d_1,1}^{n+1} - q_{d_1,0}^{n+1}}{\Delta s_{d_1}}, \quad (99)$$

$$Y_6 = \frac{(A_{d_2,0}^{n+1} + A_{d_2,1}^{n+1}) - (A_{d_2,0}^n + A_{d_2,1}^n)}{2\Delta t} + \frac{q_{d_2,1}^{n+1} - q_{d_2,0}^{n+1}}{\Delta s_{d_2}}, \quad (100)$$

and the pressures $p_{M,N_s}^{n+1}(A_{M,N_s}^{n+1})$, $p_{d_1,0}^{n+1}(A_{d_1,0}^{n+1})$ and $p_{d_2,0}^{n+1}(A_{d_2,0}^{n+1})$ depend on the corresponding areas through elastic model. The unknown variables are

$$\mathbf{x}_b = [A_{M,N_s}^{n+1}, q_{M,N_s}^{n+1}, A_{d_1,0}^{n+1}, q_{d_1,0}^{n+1}, A_{d_2,0}^{n+1}, q_{d_2,0}^{n+1}]^T, \quad (101)$$

while the interior variables of each vessel such as A_{M,N_s-1}^{n+1} and q_{M,N_s-1}^{n+1} are obtained by integration along each vessel. This system is solved at each time step to determine the bifurcation boundary variables.

2.3.2. Multiscale coupling condition

We denote the vectors of pressure and flow rate of source points at $t = t_{n+1}$ as

$$\mathbf{p}_{cap}^{n+1} = [p_{cap}^{n+1}(\mathbf{x}_1), \dots, p_{cap}^{n+1}(\mathbf{x}_{N_{cap}})]^T, \quad (102)$$

$$\mathbf{q}^{n+1} = [q^{n+1}(\mathbf{x}_1), \dots, q^{n+1}(\mathbf{x}_{N_{cap}})]^T, \quad (103)$$

respectively, where $p_{cap}^{n+1}(\mathbf{x}_i)$ and $q^{n+1}(\mathbf{x}_i)$ are the pressure and the flow rate at $\mathbf{x} = \mathbf{x}_i$ respectively, and N_{cap} is the number of upstream vessels connected to arteriolar and venular trees. We assume the Poiseuille flow in arterioles and venules, thus $q^{n+1}(\mathbf{x}_i)$ is also the flow rate in arteriolar or venular trees, which is connected to capillaries at $\mathbf{x} = \mathbf{x}_i$. We introduce the matrix \mathbf{R} , which is composed of the equivalent resistances of arteriolar and venular trees, given by

$$\mathbf{R} = \begin{bmatrix} R_{a,eq}(\mathbf{x}_1) & & & & \\ & \ddots & & & \\ & & R_{a,eq}(\mathbf{x}_i) & & \\ & & & R_{v,eq}(\mathbf{x}_{i+1}) & \\ & & & & \ddots \\ & & & & R_{v,eq}(\mathbf{x}_{N_{cap}}) \end{bmatrix}, \quad (104)$$

where $R_{a,eq}(\mathbf{x}_i)$ denotes the the equivalent resistance of an arteriolar tree connected to capillary at $\mathbf{x} = \mathbf{x}_i$ and $R_{v,eq}(\mathbf{x}_k)$ denotes that of an venular tree connected to the capillary at $\mathbf{x} = \mathbf{x}_k$. The capillary pressures at source points are given by

$$\mathbf{p}_{cap}^{n+1} = \mathbf{M}^{cap} \mathbf{q}^{n+1} + \bar{p}_1 \mathbf{1}, \quad (105)$$

where \mathbf{M}^{cap} is the resistance matrix with element $M_{iw}^{cap} = -(1/(a+b))G(r_i, \theta_i; r_w, \theta_w)$, while the Poiseuille equation for arterioles and venules yields the following

$$\mathbf{p}_{cap}^{n+1} = \mathbf{p}^{n+1} - \mathbf{R} \mathbf{q}^{n+1}, \quad (106)$$

where the pressure vector of arteries and veins \mathbf{p}^{n+1} is given by

$$\mathbf{p}^{n+1} = [p_{1,N_s}^{n+1}, \dots, p_{N_{cap},N_s}^{n+1}]^T. \quad (107)$$

Thus the coupling condition is given by

$$\begin{cases} \mathbf{p}_{cap}^{n+1} = \mathbf{M}^{cap} \mathbf{q}^{n+1} + \bar{p}_1 \mathbf{1}, \\ \mathbf{p}_{cap}^{n+1} = \mathbf{p}^{n+1} - \mathbf{R} \mathbf{q}^{n+1}, \\ \bar{p}_{mean} = \frac{1}{S} \int_{\partial\Omega_{cap}} p_{mean} ds, \\ p_{mean}(r, \theta) = -\frac{1}{a+b} \sum_{i=1}^{N_{cap}} q_i f_1(r, \theta; r_i, \theta_i) + \bar{p}_{mean}, \\ \sum_{n=1}^{N_{cap}} q_n = 0, \end{cases} \quad (108)$$

where the pressures \mathbf{p}^{n+1} are governed by following equations in terminal vessels

$$\begin{cases} \frac{\partial A_k}{\partial t} + \frac{\partial q_k}{\partial s} = 0, & k = 1, \dots, N_{cap}, \\ p_k - p_{ext} = K \left[\left(\frac{A}{A_0} \right)^{\beta_1} - \left(\frac{A}{A_0} \right)^{\beta_2} \right], & k = 1, \dots, N_{cap}, \end{cases} \quad (109)$$

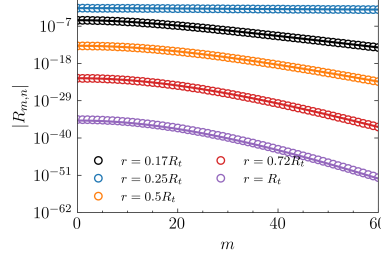


Figure 7: The dependence of radial component $R_{m,n}$ on the order m for $r_n = 0.25R_t$. Circles are the exact values of radial component computed by equation (68) while lines denote the approximation (126). Different colours correspond to various values of radial coordinate. The drainage rate is $\alpha = 2 \times 10^{-6}$ cm · s/g.

and A_k and q_k denote the area and flow rate of the terminal vessels connected to arterioles or veins, respectively.

Solving the system (108) directly is challenging due to the integral term, the conservation of mass and the nonlinear dependence of pressure on area. To simplify it, we begin with combining the first two equations in system (108), which yields the following pressure-flow relationship:

$$\mathbf{p}^{n+1} = \mathbf{R}^{cap} \mathbf{q}^{n+1} + \bar{p}_{mean} \mathbf{1}, \quad (110)$$

where $\mathbf{R}^{cap} = \mathbf{M}^{cap} + \mathbf{R}$. Solving for the flow rate vector yields to

$$\mathbf{q}^{n+1} = (\mathbf{R} + \mathbf{M}^{cap})^{-1} \mathbf{p}^{n+1} - \bar{p}_{mean} (\mathbf{R} + \mathbf{M}^{cap})^{-1} \mathbf{1}, \quad (111)$$

and then imposing the conservation of mass leads to

$$0 = \mathbf{1}^T (\mathbf{R} + \mathbf{M}^{cap})^{-1} \mathbf{p}^{n+1} - \bar{p}_{mean} \mathbf{1}^T (\mathbf{R} + \mathbf{M}^{cap})^{-1} \mathbf{1},$$

which implies that

$$\bar{p}_{mean} = \frac{1}{s_{cap}} \mathbf{1}^T (\mathbf{R} + \mathbf{M}^{cap})^{-1} \mathbf{p}^{n+1}, \quad (112)$$

with $s_{cap} = \mathbf{1}^T (\mathbf{R} + \mathbf{M}^{cap})^{-1} \mathbf{1}$. Substituting the expression of \bar{p}_{mean} into the equation (110), we obtain

$$\mathbf{p}^{n+1} = \mathbf{R}^{cap} \mathbf{q}^{n+1} + \frac{1}{s_{cap}} \mathbf{1}^T (\mathbf{R} + \mathbf{M}^{cap})^{-1} \mathbf{p}^{n+1}, \quad (113)$$

which consists of two unknown vectors \mathbf{p}^{n+1} and \mathbf{q}^{n+1} . The mass-conservation is discretized as that for CRA inlet and bifurcation boundary such that for each artery or vein,

$$q_{k,N_s}^{n+1} = q_{k,N_s-1}^{n+1} - \frac{\Delta s_k}{2\Delta t} \left[(A_{k,N_s-1}^{n+1} + A_{k,N_s}^{n+1}) - (A_{k,N_s}^n + A_{k,N_s-1}^n) \right], \quad (114)$$

where $k = 1, \dots, N_{cap}$. Given that flows in arterioles and venules are assumed as Poiseuille flow, the flow rates in arteriolar and venular trees are equal to those at boundaries of terminal vessels, that is $q^{n+1}(\mathbf{x}_k) = q_{k,N_s}^{n+1}$. This enables to express \mathbf{q}^{n+1} as

$$\mathbf{q}^{n+1} = -\mathbf{B} [(\mathbf{A}_{N_s}^{n+1} + \mathbf{A}_{N_s-1}^{n+1}) - (\mathbf{A}_{N_s}^n + \mathbf{A}_{N_s-1}^n)] + \mathbf{f}^{n+1}, \quad (115)$$

where area vectors are given by

$$\mathbf{A}_{N_s}^{n+1} = [A_{1,N_s}^{n+1}, \dots, A_{N_{cap},N_s}^{n+1}]^T, \quad (116)$$

$$\mathbf{A}_{N_s-1}^{n+1} = [A_{1,N_s-1}^{n+1}, \dots, A_{N_{cap},N_s-1}^{n+1}]^T, \quad (117)$$

$$\mathbf{A}_{N_s}^n = [A_{1,N_s}^n, \dots, A_{N_{cap},N_s}^n]^T, \quad (118)$$

$$\mathbf{A}_{N_s-1}^n = [A_{1,N_s-1}^n, \dots, A_{N_{cap},N_s-1}^n]^T \quad (119)$$

the matrix \mathbf{B} is given by

$$\mathbf{B} = \begin{bmatrix} \Delta s_1 / (2\Delta t) & & & \\ & \ddots & & \\ & & \ddots & \\ & & & \Delta s_{N_{cap}} / (2\Delta t) \end{bmatrix}, \quad (120)$$

and \mathbf{f}^{n+1} is given by

$$\mathbf{f}^{n+1} = [q_{1,N_s-1}^{n+1}, \dots, q_{N_{cap},N_s-1}^{n+1}]^T. \quad (121)$$

The numerical implementation for capillary-tissue coupled system is thus given by

$$\begin{cases} \mathbf{p}^{n+1}(\mathbf{A}_{N_s}^{n+1}) = -\mathbf{R}^{cap} \mathbf{B} (\mathbf{A}_{N_s}^{n+1} + \mathbf{A}_{N_s-1}^{n+1} - \mathbf{A}_{N_s}^n - \mathbf{A}_{N_s-1}^n) + \mathbf{R}^{cap} \mathbf{f}^{n+1} + \overline{p_{mean}} \mathbf{1}, \\ p_{k,N_s}^{n+1} - p_{ext} = K \left[\left(\frac{A_{k,N_s}^{n+1}}{A_0} \right)^{\beta_1} - \left(\frac{A_{k,N_s}^n}{A_0} \right)^{\beta_2} \right], \quad k = 1, \dots, N_{cap}, \end{cases} \quad (122)$$

where the boundary average is given by equation (112). This system is solved at each time step to obtain $\mathbf{A}_{N_s}^{n+1}$, from which \mathbf{q}^{n+1} is computed using equation (115).

3. Results

In the followings, we first analyse the convergence of the series solution for exchange pressure, which together with the analysis for its truncation error ensure the robustness and accuracy of the model. Second, the model is simulated with a constant baseline CRA pressure and the results are validated against experimental data and established models. Third, effects of crucial parameters, including permeabilities and drainage rate, are explored with constant CRA inlet pressure. Parameter values for model validation and the exploration of crucial parameters are summarized in Table 1. Finally, we simulate the pulsatile flow with a cardiac-cycle pressure profile at CRA inlet.

Parameter	Value	References
<i>Viscosity model</i>		
Viscosity of plasma, η_p	1.2 cP	[29, 30, 31]
<i>Elastic model</i>		
Young modulus, E	10^6 g/cm/s ²	[14]
Thickness of the vessel wall, h	5×10^{-4} cm	[14]
IOP	16 mmHg	[46, 9, 47]
<i>L-system</i>		
Radius of CRA	165 ± 15 μ m	[48, 34, 49]
Radius of CRV	196 ± 15 μ m	[50]
Length to diameter ratio, ξ	18 ± 3	[34]
Asymmetric ratio, v_a	1 for $d_v > 50$ μ m and 0.8 for $d_v \leq 50$ μ m	[34]
Junction exponent, γ	2.1 for $d_v > 50$ μ m and 2 for $d_v \leq 50$ μ m	[34]
<i>Structured tree model</i>		
Length to diameter ratio, ξ	23	[12, 14]
Asymmetric ratio, v_a	0.8	[34, 12]
Junction exponent, γ	2	[14]
<i>Capillary-tissue coupled system</i>		
Blood viscosity in capillary, μ_{cap}	computed by the viscosity model	
Interstitial fluid viscosity in tissue, μ_t	0.7 cP	Estimated
Capillary permeability, k_{cap}	$2 \times 10^{-11} - 2 \times 10^{-9}$ cm ²	[21]
Tissue permeability, k_t	$2 \times 10^{-14} - 2 \times 10^{-12}$ cm ²	[21]
Drainage rate, α	$2 \times 10^{-12} - 2 \times 10^{-5}$ cm · s/g	Estimated
<i>Boundary conditions at CRA and CRV</i>		
CRA inlet pressure, $p_{in,CRA}$	45 - 77 mmHg	[15, 13, 46]
CRV outlet pressure, $p_{out,CRV}$	16 mmHg	[15, 13, 46]

Table 1: The parameters for the hemodynamics in retinal microcirculation.

3.1. Convergence of the series solution for exchange pressure

The solution for p_{exch} is constructed by superimposing the contributions from all source points, where the kernel f_{exch} at each source is expressed as an infinite series (65). For practical computation, the series is truncated. The truncated series must converge if the model is to be robust and accurate.

In order to analyse its convergence, f_{exch} is decomposed into two components as

$$f_{exch} = s_1 + s_2, \quad (123)$$

where

$$s_1 = \frac{1}{2\pi} \sum_{m=-\infty}^{\infty} I_m(\lambda r_{<}^n) \frac{K'_m(\lambda R_t)}{I'_m(\lambda R_t)} I_m(\lambda r_{>}^n) \exp[im(\theta - \theta_n)], \quad (124)$$

$$s_2 = -\frac{1}{2\pi} \sum_{m=-\infty}^{\infty} I_m(\lambda r_{<}^n) K_m(\lambda r_{>}^n) \exp[im(\theta - \theta_n)]. \quad (125)$$

The series s_2 is the free-space solution which is analysed in Appendix E, describing the fundamental interaction between a source and a field point in an infinite domain, while s_1 can be interpreted as a boundary correction term, which enforces the no-flux boundary condition at the finite tissue boundary. As discussed in Appendix D, the terms in s_1 become negligible compared to those in s_2 for large m , which implies the following approximation for radial component:

$$R_{m,n}(r) \simeq -I_m(\lambda r_{<}^n) K_m(\lambda r_{>}^n), \quad (126)$$

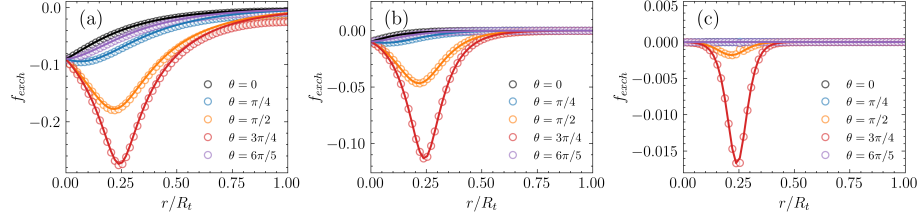


Figure 8: The behaviour of f_2 on r/R_t with $r_n = 0.25R_t$ and $\theta_n = 3\pi/2$. Circles are results of the truncation (78) with order $M = 26$, while lines are the values of approximation (128). Different colours correspond to various values of θ . The tissue permeability is set as $k_t = 2 \times 10^{-12} \text{ cm}^2$. (a) Value of drainage rate is of $\alpha = 2 \times 10^{-9} \text{ cm} \cdot \text{s/g}$. (b) Value of drainage rate is of $\alpha = 2 \times 10^{-8} \text{ cm} \cdot \text{s/g}$. (c) Value of drainage rate is of $\alpha = 2 \times 10^{-7} \text{ cm} \cdot \text{s/g}$. Other parameter values are $k_{cap} = 2 \times 10^{-9} \text{ cm}^2$ and $k_t = 2 \times 10^{-12} \text{ cm}^2$.

and as a result f_{exch} is effectively approximated by s_2 . The radial component depends on the parameter $\lambda = \sqrt{\alpha(1/a + 1/b)}$, thus its value varies with α and $1/a + 1/b$. Thus we explore the accuracy of approximation (126) with varying α and fixed permeabilities.

Figure 6 displays the dependence of radial component on the order m , where circles denote the exact values from equation (68) and lines represent the approximation (126). The approximation (126) is nearly identical to the exact value across various values of radial variable, even yielding a good estimate at $r = R_t$. These results also show that $|R_{0,n}(r)|$ could be relatively small as drainage rate increases. The approximation remains accurate as drainage rate becomes larger, as shown in figure 7. These results demonstrate that the expression (126) provides an excellent estimate for the radial component despite parameter variations, and thus the convergence of f_{exch} is equivalent to that of series s_2 .

The convergence of s_2 can be established via the following addition formula for modified Bessel functions:

$$K_0(\lambda\xi_n) = \sum_{m=-\infty}^{\infty} I_m(\lambda r_<^n) K_m(\lambda r_>^n) \exp[im(\theta - \theta_n)], \quad (127)$$

where $\xi_n = \sqrt{r^2 + r_n^2 - 2rr_n \cos(\theta - \theta_n)}$ is the distance between field point and source point. This identity could be the counterpart of Graf addition formula for Bessel functions [51], and is briefly proved in Appendix E. The addition formula for modified Bessel functions implies that the infinite series for f_{exch} sums to

$$f_{exch}(r, \theta; r_n, \theta_n) \simeq -\frac{1}{2\pi} K_0(\lambda\xi_n), \quad (128)$$

thus the series solution for f_{exch} converges asymptotically.

Figure 8 illustrates the behaviour of f_{exch} across r/R_t for various values of parameters, where circles denote the truncation of f_{exch} with truncation order $M = 26$ and lines represent the free-space approximation (128). For three

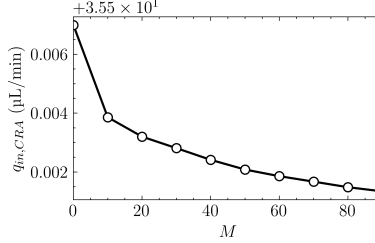


Figure 9: The dependence of total flow on truncation order M .

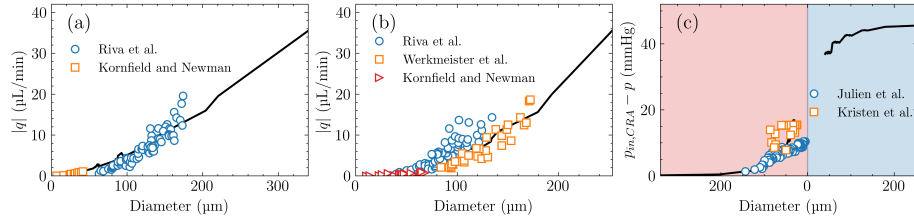


Figure 10: Flow rate and pressure difference distributions in arteries and veins. Lines denote the results of multiscale model and markers denote experimental data [1, 50, 52] and predictions of other models [14, 53]. Other parameters are $k_{cap} = 2 \times 10^{-9} \text{ cm}^2$, $k_t = 2 \times 10^{-12} \text{ cm}^2$ and $\alpha = 2 \times 10^{-9} \text{ cm} \cdot \text{s/g}$. (a) Flow rate distributions in arteries. (b) Flow rate distributions in veins. (c) Pressure difference distributions in arteries (red region) and veins (blue region).

values of drainage rate, the free-space approximation matches the truncation well, except at angular position close to θ_n .

These results, on the one hand, demonstrate the asymptotic convergence of f_{exch} . On the other hand, they also suggest how to model tissue with complicated, irregular shape. The capillary-tissue coupled system can be decoupled into pressure sum p_{mean} and pressure difference p_{exch} . The pressure sum, which might be sensitive to the boundary, can be solved numerically, while the pressure difference, which governs perfusion, can be effectively approximated using the free-space solution.

3.2. Accuracy of proposed multiscale model

We further establish the model's numerical robustness by exploring the dependence of total flow on truncation order. To assess the accuracy of our model, we then validate the model's predictions against experimental data and those of established models. The CRA inlet pressure is set to a constant baseline value of $p_{in,CRA} = 62 \text{ mmHg}$ which is the averaged pressure over one cardiac cycle approximately [9], while the CRV outlet pressure is set as $p_{out,CRV} = 16 \text{ mmHg}$.

The total flow in the retinal microcirculation is the flow rate at CRA inlet, and we denote it as $q_{in,CRA}$. Figure 9 shows total flow as a function of truncation order M . The value of $q_{in,CRA}$ exhibits convergence, with a minimal variation of approximately 0.006 μL/min across the entire range of M . Thus the model could be accurate with only a few terms in the truncation of series solution.

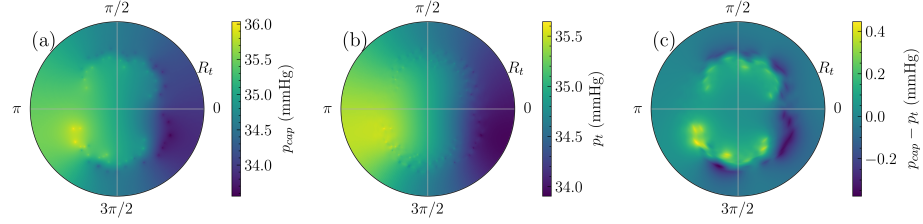


Figure 11: Capillary pressure, tissue pressure and exchange pressure. (a) Capillary pressure. (b) Tissue pressure. (c) Exchange pressure.

Figure 10(a) and (b) show the distributions of averaged flow rate in arteries and veins, respectively, where lines denote the results of multiscale model and markers represent experimental data [50, 52, 1]. Our model shows strong agreement with experimental data for artery diameters below 190 μm . For larger arteries, our model predicts smaller flow rate compared to experimental data, which might result from the overestimation of equivalent resistance in the structured trees used for resistive boundary conditions [14]. The flow rates in veins are distributed more sparsely, and our model predictions lie within the observed range of these measurements. Pressure differences between the entry of CRA and the output of each vessel are shown in figure 10(c), where results for arteries and veins are displayed in red and blue regions, respectively, with markers denote the numerical data from other models [14, 53]. Our model agrees well with 3D model for arterial diameter below 60 μm , and with established 1D model for larger arteries.

Figure 11(a), (b) and (c) display the capillary pressure, tissue pressure and their difference, respectively. Since the maximum of capillary pressure is larger than that of tissue pressure and pressures are balanced over the tissue, the pressure difference varies from -0.2 mmHg to 0.4 mmHg, with a larger positive maximum indicating the main filtration area. Although the spatial distributions of capillary and tissue pressures in figure 11(a) and (b) appear similar, capillary pressure maintain consistently higher amplitudes, resulting in the fluid exchange between them.

3.3. Model explanation for broad permeability distribution by capillary-modulated regulation

Existing experimental data reveal considerable variation in retinal hydraulic conductivity, spanning two orders of magnitude difference [54, 55, 6]. Understanding how this variability affects retinal hemodynamics is thus intriguing. We next explore the total flow, averaged pressure as well as the averaged exchange pressure with varying permeabilities. The CRA inlet pressure is set to a constant baseline value of $p_{in,CRA} = 62$ mmHg, while the CRV outlet pressure is set as $p_{out,CRV} = 16$ mmHg.

Figure 12(a) shows the dependence of total flow on capillary permeability for different tissue permeabilities, which is $k_t = 2 \times 10^{-12} \text{ cm}^2$, $k_t = 2 \times 10^{-13} \text{ cm}^2$

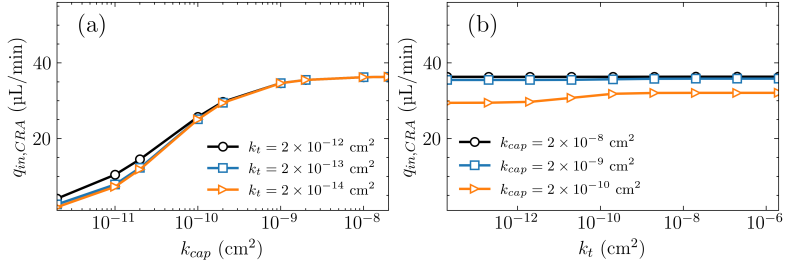


Figure 12: The dependence of total flow on capillary and tissue permeabilities. Other parameter values remains the same as those for simulations with varying CRA inlet pressure. (a) Total flow as a function of capillary permeability. Black, blue and orange lines correspond to $k_t = 2 \times 10^{-12} \text{ cm}^2$, $k_t = 2 \times 10^{-13} \text{ cm}^2$ and $k_t = 2 \times 10^{-14} \text{ cm}^2$, respectively. (b) Total flow as a function of tissue permeability. Black, blue and orange lines correspond to $k_{cap} = 2 \times 10^{-8} \text{ cm}^2$, $k_{cap} = 2 \times 10^{-9} \text{ cm}^2$ and $k_{cap} = 2 \times 10^{-10} \text{ cm}^2$, respectively.

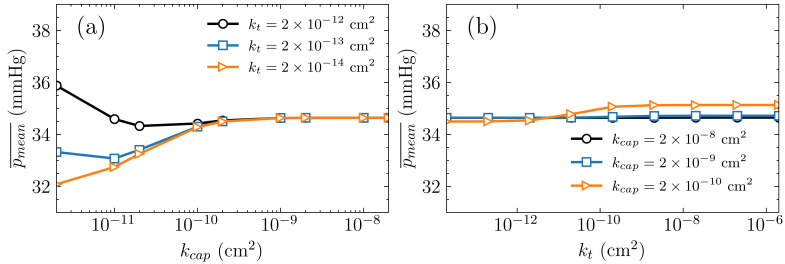


Figure 13: Domain-averaged pressure as the function of permeabilities. (a) Averaged pressure versus capillary permeability for different tissue permeabilities. (b) Averaged pressure versus tissue permeability for different capillary permeabilities.

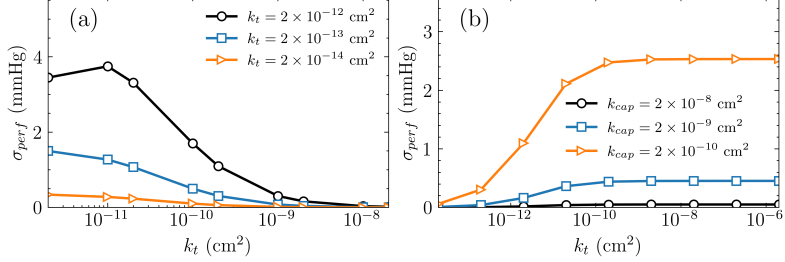


Figure 14: Domain-averaged exchange pressure as the function of permeabilities. (a) Averaged exchange pressure versus capillary permeability for different tissue permeabilities. (b) Averaged exchange pressure versus tissue permeability for different capillary permeabilities.

and $k_t = 2 \times 10^{-14}$ cm² denoted by black, blue and orange lines, respectively. All three curves exhibit similar behaviour, where total flow increases with k_{cap} up to 10^{-9} cm² approximately and plateaus near 18 μ L/min for higher values. This saturation suggests that capillary conductance significantly affects retinal dynamics only at low permeability values. In contrast, as shown by black line in figure 12(b), total flow is far less sensitive to k_t , especially when $k_{cap} = 2 \times 10^{-10}$ cm², where flow remains near the saturated value 18 μ L/min despite changes in k_t . For higher capillary permeability, tissue permeability has modest effects shown by blue and orange lines, though still with less magnitude than variations in k_{cap} .

In order to characterise the global pressure distributions, we analyse their domain-averaged quantities. The average of capillary pressure is given by

$$\overline{p_{cap}} = \overline{p_{mean}} - \frac{b}{a} \overline{p_{exch}} = \overline{p_{mean}}, \quad (129)$$

and by the identity (37) we obtain

$$\overline{p_t} = \overline{p_{cap}} = \overline{p_{mean}}. \quad (130)$$

Thus the domain-averaged capillary, tissue and mean pressures are identical. For the fluid exchange we define following metric

$$\sigma_{perf} = \frac{1}{|\Omega_t|} \int_{\Omega_t} |p_{cap} - p_t| d\mathbf{x}, \quad (131)$$

which quantifies the averaged exchange pressure since $p_{exch} = p_{cap} - p_t$. Using equation (78) it can be expressed as

$$\sigma_{perf} = \frac{1}{\pi^2 R_t^2 a} \int_0^{2\pi} \int_0^{R_t} \left| \sum_{n=1}^{N_{cap}} q_n \left[\frac{R_{0,n}}{2} + \sum_{m=1}^M R_{m,n} \cos[m(\theta - \theta_n)] \right] \right| r dr d\theta \quad (132)$$

We next compute σ_{perf} numerically with truncation order $M = 26$.

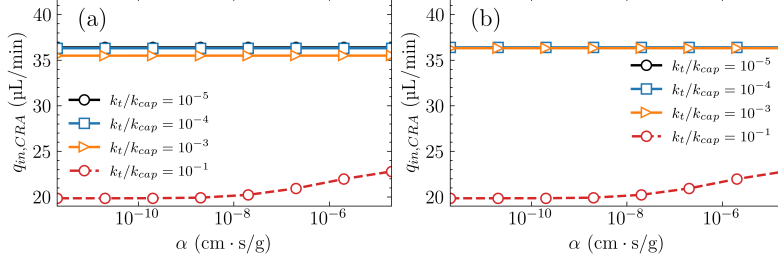


Figure 15: Total flow as a function of drainage rate for various permeability ratios. Line colours correspond to different permeability ratios. Solid lines correspond to ratios smaller than 10^{-3} , while red dashed lines correspond $k_{cap} = 4 \times 10^{-10} \text{ cm}^2$ and $k_t = 4 \times 10^{-11} \text{ cm}^2$, i.e., $k_t/k_{cap} = 10^{-1}$. (a) Tissue permeability is $k_t = 2 \times 10^{-12} \text{ cm}^2$. (b) Tissue permeability is $k_t = 2 \times 10^{-11} \text{ cm}^2$.

Figure 13 displays the domain-averaged pressures as functions of permeabilities. It is interesting that, as shown in figure 13(a), although averaged pressure converges to approximately 35 mmHg as k_{cap} increases for all values of k_t , the curve for largest k_t decays toward this value while the others approach toward it non-monotonically. In figure 13(c) the averaged pressure increases with k_t with much smaller increments, and the sensitivity of \overline{p}_{mean} to k_t decreases with k_{cap} .

Figure 14 shows the averaged exchange pressures as functions of permeabilities. The averaged exchange pressure decreases with k_{cap} generally, while the decrease amplitude increases with k_t .

These results reveal several interesting phenomena and essential properties of retinal hemodynamics. First, the sensitivities of analysed variables to capillary permeability show that k_{cap} is crucial in regulating retinal hemodynamics, while k_t plays a secondary role. Second, the saturation of total flow at higher k_{cap} might explain why experimental observations show such widely varying values of retinal hydraulic conductivity. Notably, the saturation occurs at $k_{cap} = 10^{-9} \text{ cm}^2$, which is within the physiological range [21]. Moreover the monotonic and non-monotonic convergences of averaged pressure reveal the built-in self-regulation mediated by capillary permeability, where retinal hemodynamics automatically approach homeostasis as capillary permeability increases, despite variations in tissue permeability, and demonstrate robust passive control mechanisms of capillaries.

3.4. Model exploration on drainage rate and related retinopathies

In our model, the drainage rate $\alpha = L_h \times S$ reflects the combined effect of capillary wall hydraulic conductivity L and exchange surface area S . An increase in L_h could be related to BRB dysfunction, while a change in S could arise from capillary dilation or pathological angiogenesis. Both changes underlie some retinopathies such as DR, macular edema and retinal vascular occlusions. More generally, α can be considered as a lumped parameter that includes crucial resistive or geometric determinants of fluid exchange, and its elevation could

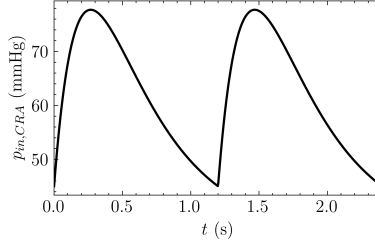


Figure 16: The pulsatile pressure profile at CRA inlet.

correspond to various diseases in retina. We thus explore how retinal hemodynamics changes with the elevated drainage rate. The CRA inlet pressure is set to a constant baseline value of $p_{in,CRA} = 62$ mmHg, while the CRV outlet pressure is set as $p_{out,CRV} = 16$ mmHg.

The retinal hemodynamics is determined by capillary pressure, $p_{cap} = p_{mean} - (b/a)p_{exch}$, which is composed of p_{mean} and p_{exch} . Only the latter, p_{exch} , depends on drainage rate through the parameter λ , whose amplitude is scaled by the factor b/a . Given fixed viscosities μ_{cap} and μ_t , the value of b/a varies with k_t/k_{cap} . Permeabilities and the ratio between them thus govern the effects of α on retinal hemodynamics.

Figure 15(a) and (b) display the dependence of total flow on drainage rate for various ratios k_t/k_{cap} , with fixed tissue permeability values of 2×10^{-12} cm 2 and 2×10^{-11} cm 2 , respectively. Different colours correspond to different permeability ratios. The total flow is insensitive to drainage rate as $k_t/k_{cap} \leq 10^{-3}$, as shown by the nearly identical black, blue and orange lines in figure 15(a). As tissue permeability become larger the total flow is also independent of k_t/k_{cap} , and it is illustrated in figure 15(b) where curves are closer. To distinguish the effects of λ from the ratio k_t/k_{cap} we set $k_{cap} = 4 \times 10^{-11}$ cm 2 and $k_t = 4 \times 10^{-12}$ cm 2 , which yields similar range for λ as those for solid lines but with higher permeability ratio of 10^{-1} , and the results are denoted by red dashed lines in figure 15(a) and (b). In this situation, total flow remains constant as $\alpha \leq 2 \times 10^{-9}$ cm · s/g but increases for higher drainage rates, which is distinct from the insensitivity observed as $k_t/k_{cap} \leq 10^{-3}$.

These results demonstrate two distinct hemodynamic regimes, with the ratio k_t/k_{cap} , correspondingly b/a , as a crucial parameter. For low ratios, i.e., $k_t/k_{cap} \leq 10^{-3}$, capillaries are more conductive than tissue and the changes in capillary-tissue coupling, i.e., drainage rate, cannot significantly affect the total flow. At higher ratios, two systems become dynamically coupled and the flow becomes sensitive to drainage rate. This indicates that relative hydraulic resistance, not absolute permeability values, fundamentally determines whether the drainage rate can affect the hemodynamics in retina, revealing a mechanism for homeostasis against retinopathies.

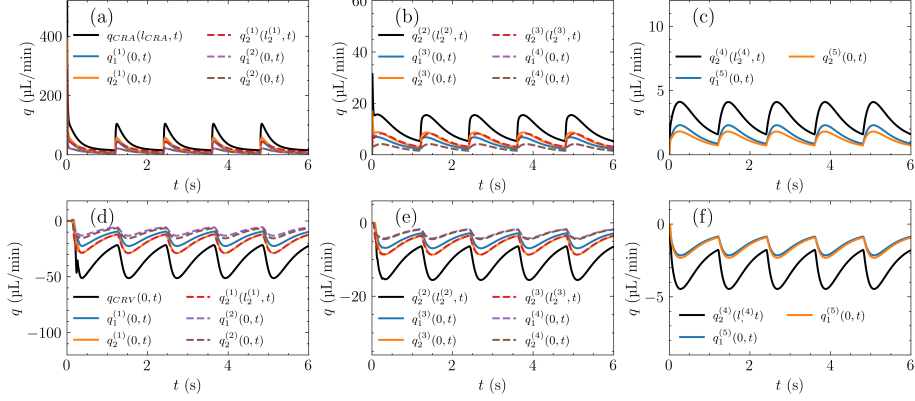


Figure 17: The temporal evolution of flow rate at bifurcation boundaries of arterial and venous trees. (a)-(c) Evolutions of flow rates in arterial tree. (d)-(f) Evolutions of flow rates in venous tree.

3.5. Model exploration with pulsatile arterial pressure

The CRA inlet pressure could exhibit significant variation due to cardiac pulsation, while the CRV outlet pressure remains almost constant [9]. We next explore the retinal hemodynamics with pulsatile arterial pressure at CRA inlet. A cardiac cycle period of $T = 1.2$ is adopted, with peak systolic pressure at $t_p = 0.268$ s. In the first period the variation profile is constructed using a shifted function $t \exp(-3.6t)$, whose shape is similar to a pulse profile [24]. The waveform is then scaled to produce physiologically relevant values: average pressure of 62.16 mmHg approximately, with systolic and diastolic pressures of 77 mmHg and 45 mmHg, respectively. The pressure profile at CRA inlet is shown figure 16.

Figure 17 shows the temporal evolution of flow rate at bifurcation boundaries in arterial and venous trees. Flow rate of vessels are denoted as $q_k^{(n)}$, where n is the level of bifurcation boundary and $k = 1, 2$ indicates the daughter vessel index, with their lengths following similar notation. Figure 17(a)-(c) show the flow through the hierarchy of arterial bifurcations. In figure 17(a), solid line show the flow rates at first-level bifurcation, including $q_{CRA}(l_{CRA}, t)$ for CRA and $q_1^{(1)}(0, t)$ and $q_2^{(1)}(0, t)$ for its two daughter arteries, while dashed lines denote the second-level flows from the secondary daughter artery in the first-level bifurcation. Figure 17(b) advances to third-level flows (solid lines) and forth-level flows (dashed lines) from the secondary branch in the upper level bifurcation. Figure 17(c) displays flow rates at fifth level bifurcation. The evolution of flow rate in veins is shown in figure 17(d)-(f), following the same descending order as that for arteries. Flows in CRA and CRV exhibit initial transients. Arterial flows all show pulsatile oscillations similar to the CRA inlet pressure, but with different amplitudes of variations, while venous flows follow simiar pulsatility but with negative values indicating flow direction. The variation is largest in

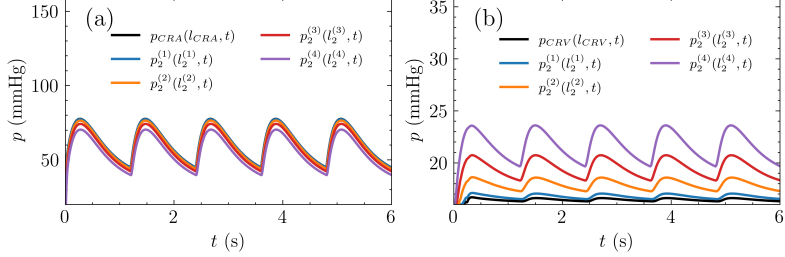


Figure 18: The evolution of pressure at bifurcation boundaries of arterial and venous trees.
(a) Evolutions of pressures in arterial trees (b) Evolution of pressures in venous tree.

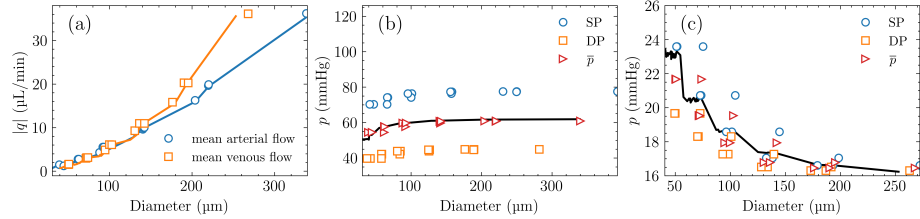


Figure 19: Pulsatile flow rates and pressures as functions of diameter. (a) Averaged pulsatile flow rates. The mean arterial and venous flows are denoted by blue and orange markers, while the distributions in steady flow are denoted by solid lines and used for baseline. (b) and (c) Arterial pressures. The SP, BP and mean pressure are denoted by blue, orange and red markers, and the pressure distribution with constant CRA inlet pressure is denoted by black line. (c) Venous pressures, using the same conventions as in (b).

the CRA, secondary in the CRV, and become damped in distal arteries and veins, with minimal oscillation at the fifth-level bifurcations.

Figure 18 shows the temporal evolution of the pressure in these vessels. Since vessels connected to the same bifurcation boundary have identical pressure, only the pressure in mother vessel at each bifurcation are shown. The variation of CRA is largest, and that of CRV is smallest. The pressure waveforms in veins are more distorted than in arteries. Moreover the pressure amplitude is generally larger in arteries than in veins, which results from the greater wall stiffness of arteries.

The flow rates and pressures shown in figure 17 and 18 are averaged and compared to those in steady flow. Figure 19(a) shows the mean arterial and venous flows, denoted by blue and orange markers, respectively. The flow rate distributions for arteries and veins in steady flow are displayed in blue and orange lines, respectively. The mean arterial and venous flows under pulsatile conditions closely match the solutions in steady flow, which results from the longer diastolic phase as well as the time-averaged CRA inlet pressure that is nearly identical to the constant CRA inlet pressure in steady flow. Figure 19(b) and (c) show the systolic pressure (SP), diastolic pressure (BP) and mean pressure \bar{p} as functions of the diameter in arteries and veins, respectively. The SP,

	$q_{in,CRA}$	$p_{in,CRA}$	$q_{out,CRV}$	$p_{out,CRV}$
Steady flow	35.50 $\mu\text{L}/\text{min}$	62 mmHg	-35.69 $\mu\text{L}/\text{min}$	16 mmHg
Pulsatile flow	36.05 $\mu\text{L}/\text{min}$	62.16 mmHg	-36.24 $\mu\text{L}/\text{min}$	16 mmHg

Table 2: The flow rates and pressures at CRV outlet and CRA inlet.

BP and mean pressure are denoted by blue, orange and red markers, respectively. As a baseline, the pressure distribution under a constant CRA inlet pressure $p_{in,CRA} = 62$ mmHg is shown by black line. All arterial pressures in steady and pulsatile flows generally increase with diameter but non-monotonically, which indicates the dependence of pressures not only on the diameter but also the distance from the CRA inlet [14]. Venous pressures decrease with diameter and the decreasing magnitude is smaller than the increasing magnitude in arteries. Moreover, both arterial and venous pressures align closely to corresponding steady distributions.

Table 2 summarizes the flow rate and pressure at CRA inlet and CRV outlet. Values for pulsatile flow are averaged over one cardiac cycle. Under steady flow conditions, the flow rate at the CRA inlet is nearly identical to that at the CRV outlet, with a small difference of 0.19 $\mu\text{L}/\text{min}$, showing the conservation of mass and the robustness of our model. In pulsatile flow, the magnitudes of averaged flow rates at both CRA inlet and CRV outlet for pulsatile flow are slightly larger than in steady condition due to the higher time-averaged CRA inlet pressure. The conservation of mass is also satisfied since the flow at CRA inlet and CRV outlet are almost identical.

4. Discussion and conclusion

This work proposes a multiscale computational model for modelling hemodynamics in retinal microcirculation, by extending previous work on tree-type vasculature flow models for artery and vein and porous medium-type of model for tissues. We have developed a fully coupled flow model that links artery-vein-capillary-tissue in a unified framework where two Darcy models for the capillary and tissue are coupled with each other as well as with two vascular tree models for the arterial and venous part of the retinal circulation. Our approach is based on widely-accepted physical principles, cf. [18], with necessary simplifications.

Another key novelty of our approach is the derivation and implementation of the analytic solution for capillary-tissue coupled system, which extends previous works that use the analytic solution for capillary flow in multiscale modelling [19, 22, 23]. In particular the 1D model [14] is adopted for the flow in arterial and venous trees, while capillary bed and surrounding tissue are treated as interacting porous media using coupled Darcy models. The capillary-tissue coupled system is solved analytically by using a decoupling transformation, which separates governing equations into two components, i.e., mean pressure and exchange pressure components. The solutions for capillary and tissue pressures are expressed as the combinations of logarithmic functions and infinite series

of modified Bessel functions. The convergence and truncation error of infinite series solution are analysed extensively to ensure the robustness and accuracy of the model. This also suggests a potential modelling methodology for other tissues with complicated geometries, where the boundary-sensitive mean pressure could be solved numerically while the exchange pressure, controlling local perfusion, can be effectively approximated using a free-space solution. Furthermore, we establish a dynamic coupling condition that bridges the capillary bed with upstream arterial and downstream venous flows. This multiscale coupling, including integral term and nonlinear pressure-area relation, was then simplified for efficient computation.

Our model's predictions with a constant baseline CRA inlet pressure agree well with experimental data, demonstrating its high predictive accuracy. The model's potential applications was further exemplified by exploring several physiologically relevant situations. First, we explore the effects of permeabilities. Our results indicate retinal hemodynamics is mainly affected by capillary permeability, exhibiting a saturated effect on total flow for higher permeability values, while tissue permeability plays a secondary role. This saturation demonstrates a robust, passive self-regulatory mechanism mediated by capillaries, which might explain the broad distribution of retinal hydraulic conductivity in experimental observations. Second, we explore the effects of drainage rate, which is related to various diseases in retina, underscoring the importance of the relative hydraulic resistance in fluid exchange. Finally, we simulated the pulsatile flows with a cardiac-cycle pressure profile at CRA inlet. The results show that the model could characterize pulsations of pressures and flows in arteries, veins, capillaries and tissue.

Despite its effectiveness, our model has several limitations. First, we have assumed constant permeabilities of both Darcy models for the capillary and tissue for simplicity. Work is current underway to extend our work to spatially varying permeabilities which will allow us to explore physiologically relevant questions such as the effect of non-uniform nature of the capillaries. We are also extending our model to time varying permeability of the capillary to explore the effect of neurovascular coupling. Second, we approximate the area where the retinal vasculature is distributed as a two-dimensional circular domain, and further studies could consider a three-dimensional spherical geometry which would represent the actual retinal anatomy better. Additionally, the model does not distinguish different capillary plexuses located in outer retina and inner retina [13], and this simplification could be addressed. Third, while osmotic pressure is important for fluid flow in many tissues [39], including the retina [6], our model focuses on the hemodynamics in retinal vasculature and thus neglects osmotic effects. Thus including oncotic pressures and coupling our model with models for other fluids would provide a more complete description for retinal microcirculation. Notably, several works have developed transport models for water and various organic and inorganic molecules in the optic nerve [24, 56, 57, 58, 59, 60, 61], and several fundamental properties of the transport in optic nerve has been revealed. Integrating our multiscale model with such models could provide deeper insights into retinal physiology and pathology. Finally, boundary

condition for tissue pressure enforces no fluid accumulation in the tissue, and it might not be physiologically accurate in certain pathological situations. For example, exudative macular edema is caused by the fluid accumulation in the tissue [6]. Further studies could thus explore other boundary conditions for such pathological situations.

In conclusion, the multiscale model proposed in this work provides an efficient and robust tool for exploring the hemodynamics in retinal microcirculation. Despite the necessary simplifications on which the model is based, our model generates physiologically consistent results and could thus help to understand the mechanisms of retinopathies as well as perform the computation for specific patients.

Acknowledgement. This work is supported in part by NSFC (Project number 12231004).

Appendix A. Solution to the equation of mean pressure

Enforcing the boundary condition $\nabla' f_{mean}(\mathbf{x}, \mathbf{x}') \cdot \mathbf{n}' = 2\pi R_t$ yields to

$$\frac{1}{|\mathbf{x}' - \mathbf{x}|^2} [|\mathbf{x}'|^2 + k|\mathbf{x}|^2 - (k+1)\mathbf{x}' \cdot \mathbf{x}] = 1, \quad (\text{A.1})$$

which holds for all \mathbf{x} and \mathbf{x}' if and only if $k = 1$, thus the coefficient k is uniquely determined. The constant c remains arbitrary and can be set as $c = 0$ without loss of generality. Thus the solution to the adjoint problem is

$$f_{mean}(\mathbf{x}, \mathbf{x}') = \frac{1}{2\pi} (\log |\mathbf{x}' - \mathbf{x}| + \log |\mathbf{x}' - \mathbf{x}''|). \quad (\text{A.2})$$

Then the solution for p_{mean} can be obtained via following convolution [42, 41]

$$p_{mean} = \int_{\Omega_t} f_{mean} \nabla'^2 p_{mean}(\mathbf{x}') d\mathbf{x}' + \int_{\partial\Omega_t} [p_{mean}(\mathbf{x}') \nabla' f_{mean} - f_{mean} \nabla' p_{mean}(\mathbf{x}')] \cdot \mathbf{n}' ds' \quad (\text{A.3})$$

Substituting the boundary conditions for f_{mean} and p_{mean} yields to

$$p_{mean}(\mathbf{x}) = \int_{\Omega_t} f_{mean}(\mathbf{x}, \mathbf{x}') \nabla'^2 p_{mean}(\mathbf{x}') d\mathbf{x}' + \frac{1}{S} \int_{\partial\Omega_t} p_{mean}(\mathbf{x}') ds'. \quad (\text{A.4})$$

The first integral is computed as

$$\begin{aligned} \int_{\Omega_t} f_{mean}(\mathbf{x}, \mathbf{x}') \nabla'^2 p_{mean}(\mathbf{x}') d\mathbf{x}' &= -\frac{1}{a+b} \sum_{n=1}^{N_{cap}} q_n \int_{\Omega_t} f_{mean}(\mathbf{x}, \mathbf{x}') \delta(\mathbf{x}' - \mathbf{x}_n) d\mathbf{x}' \\ &= -\frac{1}{a+b} \sum_{n=1}^{N_{cap}} q_n f_{mean}(\mathbf{x}, \mathbf{x}_n). \end{aligned} \quad (\text{A.5})$$

Appendix B. Computation of the boundary integral in consistent condition

On the boundary the integral is

$$\int_{\partial\Omega_t} f_{mean}(r, \theta; r_k, \theta_k) ds = R_t \int_0^{2\pi} f_{mean}(R_t, \theta; r_k, \theta_k) d\theta, \quad (\text{B.1})$$

and using the expression of f_1 we obtain

$$\int_{\partial\Omega_t} f_{mean}(r, \theta; r_k, \theta_k) ds = \frac{R_t}{2\pi} \int_0^{2\pi} \log(r_k^2 + R_t^2 - 2r_k R_t \cos(\theta_k - \theta)) d\theta, \quad (\text{B.2})$$

which can be written as

$$\int_{\partial\Omega_t} f_{mean}(r, \theta; r_k, \theta_k) ds = \frac{R_t}{2\pi} \left(\int_0^{2\pi} R_t^2 d\theta + \int_0^{2\pi} \log(\rho^2 + 1 - 2\rho \cos(\theta_k - \theta)) d\theta \right) \quad (\text{B.3})$$

where $\rho = r_k/R_t$. The first integral is $4\pi \log R_t$. The second integral is zero as $\rho < 1$ since the source point is inside the domain, which can be demonstrated by following computation:

$$\int_0^{2\pi} \log(\rho^2 + 1 - 2\rho \cos(\theta_k - \theta)) d\theta = \int_0^{2\pi} \log |1 - \rho \exp[i(\theta_k - \theta)]|^2 d\theta. \quad (\text{B.4})$$

Using the identity $\log |z|^2 = 2\text{Re}(\log z)$ this integral becomes

$$\int_0^{2\pi} \log(\rho^2 + 1 - 2\rho \cos(\theta_k - \theta)) d\theta = 2 \int_0^{2\pi} \text{Re}(\log(1 - \rho \exp(i\theta))) d\theta. \quad (\text{B.5})$$

For $|\rho| < 1$ the logarithm can be expanded as $\log(1 - \rho \exp(i\theta)) = -\sum_{n=1}^{\infty} \rho^n \exp(in\theta)/n$ such that the integral can be written as

$$\int_0^{2\pi} \log(\rho^2 + 1 - 2\rho \cos(\theta_k - \theta)) d\theta = -2 \int_0^{2\pi} \text{Re} \left(\sum_{n=1}^{\infty} \frac{\rho^n \exp(in\theta)}{n} \right) d\theta, \quad (\text{B.6})$$

and the integral is zero since $\int_0^{2\pi} \text{Re}(\exp(in\theta)) d\theta = 0$ for all integers $n \geq 1$. The boundary integral of f_{mean} is thus given by

$$\int_{\partial\Omega_t} f_{\text{mean}}(r, \theta; r_n, \theta_n) ds = 2R_t \log R_t. \quad (\text{B.7})$$

Appendix C. Solution to the adjoint problem of exchange pressure

The continuity of the function f_{exch} at $r = r_n$ provides that

$$R_m(r)|_{r=r_n^+} - R_m(r)|_{r=r_n^-} = 0, \quad (\text{C.1})$$

and the discontinuity of the derivative of f_{exch} implies that

$$\frac{dR_m(r)}{dr} \bigg|_{r=r_n^+} - \frac{dR_m(r)}{dr} \bigg|_{r=r_n^-} = \frac{1}{r_n}. \quad (\text{C.2})$$

Moreover imposing the no flux boundary condition yields to

$$\frac{dR_m(r)}{dr} \bigg|_{r=R_t} = 0. \quad (\text{C.3})$$

The boundary condition $dR_m(r)/dr|_{r=R_t} = 0$ provides that

$$C_m = -\frac{I'_m(\lambda R_t)}{K'_m(\lambda R_t)} B_m, \quad (\text{C.4})$$

and the continuity of $R_m(r)$ yields to

$$A_m = \left[1 - \frac{I'_m(\lambda R_t)}{K'_m(\lambda R_t)} \frac{K_m(\lambda r_n)}{I_m(\lambda r_n)} \right] B_m. \quad (\text{C.5})$$

Thus the discontinuity of $dR_m(r)/dr$ at $r = r_n$ gives rise to

$$B_m \frac{I'_m(\lambda R_t)}{K'_m(\lambda R_t)} \frac{I_m(\lambda r_n)K'_m(\lambda r_n) - K_m(\lambda r_n)I'_m(\lambda r_n)}{I_m(\lambda r_n)} = \frac{1}{\lambda r_n}, \quad (\text{C.6})$$

and using the identity [62, p. 866]

$$I_m(\lambda r_n)K'_m(\lambda r_n) - K_m(\lambda r_n)I'_m(\lambda r_n) = -\frac{1}{\lambda r_n} \quad (\text{C.7})$$

we obtain

$$B_m = \frac{K'_m(\lambda R_t)}{I'_m(\lambda R_t)} I_m(\lambda r_n), \quad (\text{C.8})$$

and

$$A_m = \frac{K'_m(\lambda R_t)I_m(\lambda r_n)}{I'_m(\lambda R_t)} - K_m(\lambda r_n), \quad (\text{C.9})$$

$$C_m = -I_m(\lambda r_n). \quad (\text{C.10})$$

Appendix D. Ratio between terms

The ratio between the first term and the second term in radial component is given by

$$e_{m,n} = \left| \frac{K'_m(\lambda R_t)I_m(\lambda r_>^n)}{I'_m(\lambda R_t)K_m(\lambda r_>^n)} \right|. \quad (\text{D.1})$$

If m is fixed the derivative $K'_m(\lambda r)$ is negative and increasing. Then

$$e_{m,n} \leq -\frac{K'_m(\lambda R_t)I_m(\lambda r_>^n)}{I'_m(\lambda r_>^n)K_m(\lambda r_>^n)}. \quad (\text{D.2})$$

Using the inequality that [62, p. 867]

$$\frac{I'_m(\lambda r)}{I_m(\lambda r)} > \frac{m}{\lambda r}, \quad m > -1, \quad \lambda r > 0, \quad (\text{D.3})$$

the inequality can be written as

$$e_{m,n} \leq -\frac{\lambda r_>^n}{m} \frac{K'_m(\lambda R_t)}{K_m(\lambda r_>^n)}, \quad m > -1, \quad \lambda r > 0. \quad (\text{D.4})$$

Using the inequality that [62, p. 867]

$$-\frac{K'_m(\lambda r)}{K_m(\lambda r)} < \frac{m}{\lambda r} + 1, \quad m > 1/2, \quad \lambda r > 0, \quad (\text{D.5})$$

we obtain

$$e_{m,n} \leq \frac{\lambda r_{>}^n}{m} \left(\frac{m}{\lambda R_t} + 1 \right) \frac{K_m(\lambda R_t)}{K_m(\lambda r_{>}^n)}, \quad m > 1/2, \quad \lambda r > 0. \quad (\text{D.6})$$

Using the inequality (63, equation 3.4; 64, equation 2.17) that $K_m(r_1)/K_m(r_2) > (r_2/r_1)^m$ for $m > -1/2$ and $0 < r_1 < r_2$ we obtain that

$$e_{m,n} \leq \frac{\lambda r_{>}^n}{m} \left(\frac{m}{\lambda R_t} + 1 \right) \left(\frac{\lambda r_{>}^n}{\lambda R_t} \right)^m, \quad m > 1/2, \quad \lambda r > 0, \quad (\text{D.7})$$

thus for $0 \leq r < R_t$ the ratio $e_{m,n} \rightarrow 0$ as $m \rightarrow \infty$ and the first term can be neglected.

Appendix E. Proof of addition formula for infinite series

Consider following problem in two dimensions:

$$\nabla^2 f_{exch}(\mathbf{x}, \mathbf{x}_n) - \lambda^2 f_{exch}(\mathbf{x}, \mathbf{x}_n) = \delta(\mathbf{x} - \mathbf{x}_n), \quad (\text{E.1})$$

subjected to the boundary condition that $f_{exch} \rightarrow 0$ as $|\mathbf{x}| \rightarrow \infty$. In polar coordinates, with $\mathbf{x}_n = (r_n, \theta_n)$, the equation is given by equation (61). Expanding f_{exch} in a Fourier series and solving the resulting modified Bessel equation, with proper matching for the coefficients of the expansion of delta function, yields

$$f_{exch} = \frac{1}{2\pi} \sum_{m=-\infty}^{\infty} I_m(\lambda r_{<}) K_m(\lambda r_{>}) \exp[i m(\theta - \theta_n)], \quad (\text{E.2})$$

and $r_{<}^n = \min(r, r_n)$ and $r_{>}^n = \max(r, r_n)$. On the other hand, since the problem is defined on infinite domain f_{exch} is independent of angular variable. The equation becomes

$$\frac{1}{r} \frac{\partial}{\partial r} \left(r \frac{\partial f_{exch}}{\partial r} \right) - \lambda^2 f_{exch} = \frac{\delta(r - r_n) \delta(\theta - \theta_n)}{r}, \quad (\text{E.3})$$

and solving this equation with given boundary condition we obtain

$$f_{exch} = \frac{1}{2\pi} K_0 \left(\lambda \sqrt{r^2 + r_n^2 - 2rr_n \cos(\theta - \theta_n)} \right). \quad (\text{E.4})$$

Then the uniqueness of the solution implies the addition formula for modified Bessel functions.

References

- [1] T. E. Kornfield, E. A. Newman, Measurement of Retinal Blood Flow Using Fluorescently Labeled Red Blood Cells, *eNeuro* 2 (2) (2015) ENEURO.0005-15.2015. doi:10.1523/ENEURO.0005-15.2015.
URL <https://www.eneuro.org/lookup/doi/10.1523/ENEURO.0005-15.2015>

[2] G. Garhöfer, C. Zawinka, H. Resch, K. H. Huemer, L. Schmetterer, G. T. Dorner, Response of Retinal Vessel Diameters to Flicker Stimulation in Patients with Early Open Angle Glaucoma:, *J. Glaucoma* 13 (4) (2004) 340–344. doi:10.1097/00061198-200408000-00013.
URL <http://journals.lww.com/00061198-200408000-00013>

[3] J. Caprioli, A. L. Coleman, Blood Pressure, Perfusion Pressure, and Glaucoma, *Am. J. Ophthalmol.* 149 (5) (2010) 704–712. doi:10.1016/j.ajo.2010.01.018.
URL <https://linkinghub.elsevier.com/retrieve/pii/S0002939410000346>

[4] T. W. Ch'ng, C. Y. Chua, M. A. Ummi Kalsom, Y. Azhany, V. H. M. Gong, A. H. G. Rasool, A. T. Liza-Sharmini, Ocular Perfusion Pressure and Severity of Glaucoma: Is There a Link?, *J. Curr. Glaucoma Pract.* 15 (2) (2021) 78–85. doi:10.5005/jp-journals-10078-1305.
URL <https://www.jocgp.com/doi/10.5005/jp-journals-10078-1305>

[5] N. N. Osborne, R. J. Casson, J. P. M. Wood, G. Chidlow, M. Graham, J. Melena, Retinal ischemia: mechanisms of damage and potential therapeutic strategies, *Prog. Retin. Eye Res.* 23 (1) (2004) 91–147. doi:10.1016/j.preteyeres.2003.12.001.
URL <https://linkinghub.elsevier.com/retrieve/pii/S1350946203000788>

[6] A. Ruffini, M. Dvoriashyna, A. Govetto, M. R. Romano, R. Repetto, A Mathematical Model of Interstitial Fluid Flow and Retinal Tissue Deformation in Macular Edema, *Invest. Ophthalmol. Vis. Sci.* 65 (11) (2024) 19. doi:10.1167/iovs.65.11.19.
URL <https://iovs.arvojournals.org/article.aspx?articleid=2800791>

[7] J. H. Siggers, C. R. Ethier, Fluid Mechanics of the Eye, *Annu. Rev. Fluid Mech.* 44 (1) (2012) 347–372. doi:10.1146/annurev-fluid-120710-101058.
URL <https://www.annualreviews.org/doi/10.1146/annurev-fluid-120710-101058>

[8] J. Flores, J. Alastrauey, E. Corvera Poiré, A Novel Analytical Approach to Pulsatile Blood Flow in the Arterial Network, *Ann. Biomed. Eng.* 44 (10) (2016) 3047–3068. doi:10.1007/s10439-016-1625-3.
URL <http://link.springer.com/10.1007/s10439-016-1625-3>

[9] G. Guidoboni, A. Harris, S. Cassani, J. Arciero, B. Siesky, A. Amireskandari, L. Tobe, P. Egan, I. Januleviciene, J. Park, Intraocular Pressure, Blood Pressure, and Retinal Blood Flow Autoregulation: A Mathematical Model to Clarify Their Relationship and Clinical Relevance, *Invest. Ophthalmol. Vis. Sci.* 55 (7) (2014) 4105. doi:10.1167/iovs.13-13611.

URL <http://iovs.arvojournals.org/article.aspx?doi=10.1167/iovs.13-13611>

[10] P. Ganesan, S. He, H. Xu, Analysis of retinal circulation using an image-based network model of retinal vasculature, *Microvasc. Res.* 80 (1) (2010) 99–109. doi:10.1016/j.mvr.2010.02.005.
 URL <https://linkinghub.elsevier.com/retrieve/pii/S0026286210000373>

[11] B. C. Fry, E. B. Coburn, S. Whiteman, A. Harris, B. Siesky, J. Arciero, Predicting retinal tissue oxygenation using an image-based theoretical model, *Math. Biosci.* 305 (2018) 1–9. doi:10.1016/j.mbs.2018.08.005.
 URL <https://linkinghub.elsevier.com/retrieve/pii/S0025556417306831>

[12] D. Liu, N. B. Wood, N. Witt, A. D. Hughes, S. A. Thom, X. Y. Xu, Computational Analysis of Oxygen Transport in the Retinal Arterial Network, *Curr. Eye Res.* 34 (11) (2009) 945–956. doi:10.3109/02713680903230079.
 URL <http://www.tandfonline.com/doi/full/10.3109/02713680903230079>

[13] P. Causin, G. Guidoboni, F. Malgaroli, R. Sacco, A. Harris, Blood flow mechanics and oxygen transport and delivery in the retinal microcirculation: multiscale mathematical modeling and numerical simulation, *Biomech. Model. Mechanobiol.* 15 (3) (2016) 525–542. doi:10.1007/s10237-015-0708-7.
 URL <http://link.springer.com/10.1007/s10237-015-0708-7>

[14] L. Julien, S. Bonnin, M. Paques, J.-M. Fullana, One-dimensional modeling of microvascular hemodynamics in the retina using multimodal imaging, *Phys. Fluids* 35 (6) (2023) 061901. doi:10.1063/5.0152499.
 URL <https://pubs.aip.org/pof/article/35/6/061901/2894457/One-dimensional-modeling-of-microvascular>

[15] J. Rebhan, L. P. Parker, L. J. Kelsey, F. K. Chen, B. J. Doyle, A computational framework to investigate retinal haemodynamics and tissue stress, *Biomech. Model. Mechanobiol.* 18 (6) (2019) 1745–1757. doi:10.1007/s10237-019-01172-y.
 URL <http://link.springer.com/10.1007/s10237-019-01172-y>

[16] J. Malek, A. T. Azar, B. Nasralli, M. Tekari, H. Kamoun, R. Tourki, Computational analysis of blood flow in the retinal arteries and veins using fundus image, *Comput. Math. Appl.* 69 (2) (2015) 101–116. doi:10.1016/j.camwa.2014.11.017.
 URL <https://linkinghub.elsevier.com/retrieve/pii/S0898122114005859>

[17] K. C. Tripathy, A. Siddharth, A. Bhandari, Image-based insilico investigation of hemodynamics and biomechanics in healthy

and diabetic human retinas, *Microvasc. Res.* 150 (2023) 104594. doi:10.1016/j.mvr.2023.104594.
 URL <https://linkinghub.elsevier.com/retrieve/pii/S0026286223001206>

[18] R. Eisenberg, Structural analysis of fluid flow in complex biological systems, *MAIO* 4 (1) (Feb. 2023). doi:10.35119/maio.v4i1.126.
 URL <https://www.maio-journal.com/index.php/MAIO/article/view/126>

[19] R. J. Shipley, A. F. Smith, P. W. Sweeney, A. R. Pries, T. W. Secomb, A hybrid discrete–continuum approach for modelling microcirculatory blood flow, *Math. Med. Biol.* (Mar. 2019). doi:10.1093/imammb/dqz006.
 URL <https://academic.oup.com/imammb/advance-article/doi/10.1093/imammb/dqz006/5393647>

[20] U. N. A. Qohar, A. Z. Munthe-Kaas, J. M. Nordbotten, E. A. Hanson, A nonlinear multi-scale model for blood circulation in a realistic vascular system, *R. Soc. open sci.* 8 (12) (2021) 201949. doi:10.1098/rsos.201949.
 URL <https://royalsocietypublishing.org/doi/10.1098/rsos.201949>

[21] M. Fritz, T. Köppl, J. Oden, A. Wagner, B. Wohlmuth, C. Wu, A 1D–0D–3D coupled model for simulating blood flow and transport processes in breast tissue, *Int. J. Numer. Meth. Biomed. Engng.* 38 (7) (2022) e3612. doi:10.1002/cnm.3612.
 URL <https://onlinelibrary.wiley.com/doi/10.1002/cnm.3612>

[22] P. W. Sweeney, C. Walsh, S. Walker-Samuel, R. J. Shipley, A three-dimensional, discrete-continuum model of blood pressure in microvascular networks, *Int. J. Numer. Methods Biomed. Eng.* 40 (8) (2024) e3832. doi:10.1002/cnm.3832.
 URL <https://onlinelibrary.wiley.com/doi/10.1002/cnm.3832>

[23] A. d’Esposito, P. W. Sweeney, M. Ali, M. Saleh, R. Ramasawmy, T. A. Roberts, G. Agliardi, A. Desjardins, M. F. Lythgoe, R. B. Pedley, R. Shipley, S. Walker-Samuel, Computational fluid dynamics with imaging of cleared tissue and of in vivo perfusion predicts drug uptake and treatment responses in tumours, *Nat. Biomed. Eng.* 2 (10) (2018) 773–787. doi:10.1038/s41551-018-0306-y.
 URL <https://www.nature.com/articles/s41551-018-0306-y>

[24] Z. Song, S. Xu, R. Eisenberg, H. Huang, A multi-domain model for microcirculation in optic nerve: Blood flow and oxygen transport, *Physica D* 467 (2024) 134272. doi:10.1016/j.physd.2024.134272.
 URL <https://linkinghub.elsevier.com/retrieve/pii/S0167278924002239>

[25] X.-F. Wang, S. Nishi, M. Matsukawa, A. Ghigo, P.-Y. Lagrée, J.-M. Fullana, Fluid friction and wall viscosity of the 1D blood flow model, *J. Biomech.* 49 (4) (2016) 565–571. doi:10.1016/j.jbiomech.2016.01.010. URL <https://linkinghub.elsevier.com/retrieve/pii/S0021929016000191>

[26] W. Song, Q. Wei, W. Liu, T. Liu, J. Yi, N. Sheibani, A. A. Fawzi, R. A. Linsenmeier, S. Jiao, H. F. Zhang, A combined method to quantify the retinal metabolic rate of oxygen using photoacoustic ophthalmoscopy and optical coherence tomography, *Sci. Rep.* 4 (1) (2014) 6525. doi:10.1038/srep06525. URL <https://www.nature.com/articles/srep06525>

[27] J. Liu, H. Suito, A multicore parallel algorithm for multiscale modelling of an entire human blood circulation network (2024). doi:10.48550/ARXIV.2404.01680. URL <https://arxiv.org/abs/2404.01680>

[28] L. O. Müller, E. F. Toro, A global multiscale mathematical model for the human circulation with emphasis on the venous system: A GLOBAL MULTISCALE MATHEMATICAL MODEL FOR THE HUMAN CIRCULATION, *Int. J. Numer. Meth. Biomed. Engng.* 30 (7) (2014) 681–725. doi:10.1002/cnm.2622. URL <https://onlinelibrary.wiley.com/doi/10.1002/cnm.2622>

[29] A. R. Pries, T. W. Secomb, T. Gessner, M. B. Sperandio, J. F. Gross, P. Gaehtgens, Resistance to blood flow in microvessels in vivo., *Circ. Res.* 75 (5) (1994) 904–915. doi:10.1161/01.RES.75.5.904. URL <https://www.ahajournals.org/doi/10.1161/01.RES.75.5.904>

[30] T. W. Secomb, A. R. Pries, Blood viscosity in microvessels: Experiment and theory, *C. R. Phys.* 14 (6) (2013) 470–478. doi:10.1016/j.crhy.2013.04.002. URL <https://comptes-rendus.academie-sciences.fr/physique/articles/10.1016/j.crhy.2013.04.002/>

[31] N. Bappoo, L. J. Kelsey, L. Parker, T. Crough, C. M. Moran, A. Thomson, M. C. Holmes, C. S. Wyrwoll, B. J. Doyle, Viscosity and haemodynamics in a late gestation rat feto-placental arterial network, *Biomech. Model. Mechanobiol.* 16 (4) (2017) 1361–1372. doi:10.1007/s10237-017-0892-8. URL <http://link.springer.com/10.1007/s10237-017-0892-8>

[32] V. B. Kolachalama, N. W. Bressloff, P. B. Nair, C. P. Shearman, Predictive Haemodynamics in a One-Dimensional Human Carotid Artery Bifurcation. Part I: Application to Stent Design, *IEEE Trans. Biomed. Eng.* 54 (5) (2007) 802–812. doi:10.1109/TBME.2006.889188. URL <https://ieeexplore.ieee.org/document/4155000/>

[33] M. S. Olufsen, C. S. Peskin, W. Y. Kim, E. M. Pedersen, A. Nadim, J. Larsen, Numerical Simulation and Experimental Validation of Blood Flow in Arteries with Structured-Tree Outflow Conditions, *Ann. Biomed. Eng.* 28 (11) (2000) 1281–1299. doi:10.1114/1.1326031.
 URL <http://link.springer.com/10.1114/1.1326031>

[34] E. E. Brown, A. A. Guy, N. A. Holroyd, P. W. Sweeney, L. Gourmet, H. Coleman, C. Walsh, A. E. Markaki, R. Shipley, R. Rajendram, S. Walker-Samuel, Physics-informed deep generative learning for quantitative assessment of the retina, *Nat. Commun.* 15 (1) (2024) 6859. doi:10.1038/s41467-024-50911-y.
 URL <https://www.nature.com/articles/s41467-024-50911-y>

[35] M. Zamir, Arterial Branching within the Confines of Fractal L-System Formalism, *J. Gen. Physiol.* 118 (3) (2001) 267–276. doi:10.1085/jgp.118.3.267.
 URL <https://rupress.org/jgp/article/118/3/267/42446/Arterial-Branching-within-the-Confines-of-Fractal>

[36] J. Staal, M. D. Abramoff, M. Niemeijer, M. A. Viergever, B. van Ginneken, Ridge-Based Vessel Segmentation in Color Images of the Retina, *IEEE Trans. Med. Imaging* 23 (4) (2004) 501–509. doi:10.1109/TMI.2004.825627.
 URL <http://ieeexplore.ieee.org/document/1282003/>

[37] T. I. Józsa, R. M. Padmos, N. Samuels, W. K. El-Bouri, A. G. Hoekstra, S. J. Payne, A porous circulation model of the human brain for *in silico* clinical trials in ischaemic stroke, *Interface Focus* 11 (1) (2021) 20190127. doi:10.1098/rsfs.2019.0127.
 URL <https://royalsocietypublishing.org/doi/10.1098/rsfs.2019.0127>

[38] E. Vidotto, T. Koch, T. Köppl, R. Helmig, B. Wohlmuth, Hybrid Models for Simulating Blood Flow in Microvascular Networks, *Multiscale Model. Simul.* 17 (3) (2019) 1076–1102. doi:10.1137/18M1228712.
 URL <https://pubs.siam.org/doi/10.1137/18M1228712>

[39] S. Xu, B. Eisenberg, Z. Song, H. Huang, Osmosis through a Semi-permeable Membrane: a Consistent Approach to Interactions, version Number: 3 (2018). doi:10.48550/ARXIV.1806.00646.
 URL <https://arxiv.org/abs/1806.00646>

[40] J. R. Levick, C. C. Michel, Microvascular fluid exchange and the revised Starling principle, *Cardiovasc. Res.* 87 (2) (2010) 198–210. doi:10.1093/cvr/cvq062.
 URL <https://academic.oup.com/cardiovascres/article-lookup/doi/10.1093/cvr/cvq062>

[41] K. J. Kim, J. D. Jackson, Proof that the Neumann Green's function in electrostatics can be symmetrized, *Am. J. Phys.* 61 (12) (1993) 1144–1146. [doi:10.1119/1.17311](https://doi.org/10.1119/1.17311).
 URL <https://pubs.aip.org/ajp/article/61/12/1144/1054244/Proof-that-the-Neumann-Green-s-function-in>

[42] K. F. Riley, M. P. Hobson, S. J. Bence, *Mathematical Methods for Physics and Engineering*, 3rd Edition, Cambridge University Press, Cambridge, 2006. [doi:10.1017/CBO9780511810763](https://doi.org/10.1017/CBO9780511810763).
 URL <https://www.cambridge.org/highereducation/books/mathematical-methods-for-physics-and-engineering/FC466374D5B94E86D969100070CA6483>

[43] D. Ruiz-Antolín, J. Segura, A new type of sharp bounds for ratios of modified Bessel functions, *J. Math. Anal. Appl.* 443 (2) (2016) 1232–1246. [doi:10.1016/j.jmaa.2016.06.011](https://doi.org/10.1016/j.jmaa.2016.06.011).
 URL <https://linkinghub.elsevier.com/retrieve/pii/S0022247X16302402>

[44] Y. He, H. Liu, R. Himeno, A one-dimensional thermo-fluid model of blood circulation in the human upper limb, *Int. J. Heat Mass Transf.* 47 (12-13) (2004) 2735–2745. [doi:10.1016/j.ijheatmasstransfer.2003.10.041](https://doi.org/10.1016/j.ijheatmasstransfer.2003.10.041).
 URL <https://linkinghub.elsevier.com/retrieve/pii/S001793100400002X>

[45] T. Köppl, R. Helmig, *Dimension Reduced Modeling of Blood Flow in Large Arteries: An Introduction for Master Students and First Year Doctoral Students, Mathematical Engineering*, Springer International Publishing, Cham, 2023. [doi:10.1007/978-3-031-33087-2](https://doi.org/10.1007/978-3-031-33087-2).
 URL <https://link.springer.com/10.1007/978-3-031-33087-2>

[46] G. Guidoboni, A. Harris, L. Carichino, Y. Arieli, B. A. Siesky, Effect of intraocular pressure on the hemodynamics of the central retinal artery: A mathematical model, *Mathematical Biosciences and Engineering* 11 (3) (2014) 523–546. [doi:10.3934/mbe.2014.11.523](https://doi.org/10.3934/mbe.2014.11.523).
 URL <http://www.aimspress.com/article/10.3934/mbe.2014.11.523>

[47] M. Ertop, Y. T. Fulya, Y. K. Aribas, H. B. Özdemir, G. Gürelik, M. E. Atilgan, S. Özdek, Evaluation of Central and Peripheral Retinal Vascular Changes in the Fellow Eyes of Patients with Unilateral Retinal Vein Occlusions, *Turk. J. Ophthalmol.* 53 (6) (2023) 349–355. [doi:10.4274/tjo.galenos.2023.94389](https://doi.org/10.4274/tjo.galenos.2023.94389).
 URL <https://oftalmoloji.org/articles/doi/tjo.galenos.2023.94389>

[48] G. T. Dorner, E. Polska, G. Garhöfer, C. Zawinka, B. Frank, L. Schmetterer, Calculation of the diameter of the central retinal artery from noninvasive measurements in humans, *Curr. Eye Res.* 25 (6)

(2002) 341–345. doi:10.1076/ceyr.25.6.341.14231.
 URL <http://www.tandfonline.com/doi/full/10.1076/ceyr.25.6.341.14231>

[49] R. J. Hernandez, S. Madhusudhan, Y. Zheng, W. K. El-Bouri, Linking Vascular Structure and Function: Image-Based Virtual Populations of the Retina, *Invest. Ophthalmol. Vis. Sci.* 65 (4) (2024) 40. doi:10.1167/iovs.65.4.40.
 URL <https://iovs.arvojournals.org/article.aspx?articleid=2793616>

[50] C. E. Riva, J. E. Grunwald, S. H. Sinclair, B. L. Petrig, Blood velocity and volumetric flow rate in human retinal vessels, *Invest. Ophthalmol. Vis. Sci.* 26 (8) (1985) 1124–1132.

[51] M. Abramowitz, I. A. Stegun (Eds.), *Handbook of mathematical functions: with formulas, graphs, and mathematical tables*, 9th Edition, Dover books on mathematics, Dover Publ, New York, NY, 2013.

[52] R. M. Werkmeister, N. Dragostinoff, S. Palkovits, R. Told, A. Boltz, R. A. Leitgeb, M. Gröschl, G. Garhöfer, L. Schmetterer, Measurement of Absolute Blood Flow Velocity and Blood Flow in the Human Retina by Dual-Beam Bidirectional Doppler Fourier-Domain Optical Coherence Tomography, *Invest. Ophthalmol. Vis. Sci.* 53 (10) (2012) 6062. doi:10.1167/iovs.12-9514.
 URL <http://iovs.arvojournals.org/article.aspx?doi=10.1167/iovs.12-9514>

[53] A. Kristen, L. Kelsey, E. Wintermantel, B. Doyle, Fundus Image Based Blood Flow Simulation of the Retinal Arteries, in: G. R. Joldes, B. Doyle, A. Wittek, P. M. Nielsen, K. Miller (Eds.), *Computational Biomechanics for Medicine*, Springer International Publishing, Cham, 2016, pp. 143–154. doi:10.1007/978-3-319-28329-6_13.
 URL http://link.springer.com/10.1007/978-3-319-28329-6_13

[54] I. Fatt, K. Shantinath, Flow conductivity of retina and its role in retinal adhesion, *Exp. Eye Res.* 12 (2) (1971) 218–226. doi:10.1016/0014-4835(71)90094-7.
 URL <https://linkinghub.elsevier.com/retrieve/pii/0014483571900947>

[55] R. J. Antcliff, Hydraulic Conductivity of Fixed Retinal Tissue After Sequential Excimer Laser Ablation: Barriers Limiting Fluid Distribution and Implications for Cystoid Macular Edema, *Arch. Ophthalmol.* 119 (4) (2001) 539. doi:10.1001/archopht.119.4.539.
 URL <http://archopht.jamanetwork.com/article.aspx?doi=10.1001/archopht.119.4.539>

[56] Y. Zhu, S. Xu, R. S. Eisenberg, H. Huang, A Bidomain Model for Lens Microcirculation, *Biophysical Journal* 116 (6) (2019) 1171–1184. [doi:10.1016/j.bpj.2019.02.007](https://doi.org/10.1016/j.bpj.2019.02.007).
 URL <https://linkinghub.elsevier.com/retrieve/pii/S0006349519301341>

[57] Y. Zhu, S. Xu, R. S. Eisenberg, H. Huang, Membranes in Optic Nerve Models, *arXiv:2105.14411 [math]* (Jun. 2021). [doi:10.48550/arXiv.2105.14411](https://doi.org/10.48550/arXiv.2105.14411).
 URL <http://arxiv.org/abs/2105.14411>

[58] S. Xiao, H. Huang, R. Eisenberg, Z. Song, S. Xu, Potassium Clearance in Optic Nerve: A Multidomain Model, *Front. Biosci. (Landmark Ed)* 30 (7) (2025) 39722. [doi:10.31083/FBL39722](https://doi.org/10.31083/FBL39722).
 URL <https://www.imrpress.com/journal/FBL/30/7/10.31083/FBL39722>

[59] S. Xiao, H. Huang, R. Eisenberg, Z. Song, S. Xu, Glymphatic Clearance in the Optic Nerve: A Multidomain Electro-osmotic Model, version Number: 1 (2025). [doi:10.48550/ARXIV.2510.22271](https://doi.org/10.48550/ARXIV.2510.22271).
 URL <https://arxiv.org/abs/2510.22271>

[60] Y. Zhu, S. Xu, R. S. Eisenberg, H. Huang, A tridomain model for potassium clearance in optic nerve of *Necturus*, *Biophys. J.* 120 (15) (2021) 3008–3027. [doi:10.1016/j.bpj.2021.06.020](https://doi.org/10.1016/j.bpj.2021.06.020).
 URL <https://linkinghub.elsevier.com/retrieve/pii/S0006349521005075>

[61] Y. Zhu, S. Xu, R. S. Eisenberg, H. Huang, Optic nerve microcirculation: Fluid flow and electrodiffusion, *Phys. Fluids* 33 (4) (2021) 041906. [doi:10.1063/5.0046323](https://doi.org/10.1063/5.0046323).
 URL <https://pubs.aip.org/pof/article/33/4/041906/994351/Optic-nerve-microcirculation-Fluid-flow-and>

[62] Á. Baricz, D. J. Maširević, S. Ponnusamy, S. Singh, Bounds for the product of modified Bessel functions, *Aequat. Math.* 90 (4) (2016) 859–870. [doi:10.1007/s00010-016-0414-2](https://doi.org/10.1007/s00010-016-0414-2).
 URL <http://link.springer.com/10.1007/s00010-016-0414-2>

[63] Á. Baricz, Bounds for modified Bessel functions of the first and second kinds, *Proc. Edinb. Math. Soc.* 53 (3) (2010) 575–599. [doi:10.1017/S0013091508001016](https://doi.org/10.1017/S0013091508001016).
 URL https://www.cambridge.org/core/product/identifier/S0013091508001016/type/journal_article

[64] C. M. Joshi, S. K. Bissu, Inequalities for some special functions, *J. Comput. Appl. Math.* 69 (2) (1996) 251–259. [doi:10.1016/0377-0427\(95\)00042-9](https://doi.org/10.1016/0377-0427(95)00042-9).
 URL <https://linkinghub.elsevier.com/retrieve/pii/0377042795000429>